MEASURING BLOOD FLOW IN THE SKELETAL MUSCLE MICROCIRCULATION USING LASER SPECKLE FLOWMETRY

A Senior Project
presented to
the Faculty of Biomedical and General Engineering Department
California Polytechnic State University,
San Luis Obispo

In Partial Fulfillment
of the Requirements for the Degree
Bachelor of Science in Biomedical Engineering

by
Kenneth Howard Gouin III
July 2015

PROJECT INFORMATION

TITLE:	Measuring Blood Flow in the Skeletal Muscle Microcirculation using Laser Speckle Flowmetry
AUTHOR:	Kenneth Howard Gouin III
DATE SUBMITTED:	July 2015
ADVIOR:	Trevor Ryan Cardinal, Ph.D.

ABSTRACT
Measuring Blood Flow in the Skeletal Muscle Microcirculation using Laser Speckle Flowmetry
Kenneth Howard Gouin III

The presence of a native collateral circulation, which serves as a natural bypass for blood flow around an occlusion, improves prognosis for patients with ischemic diseases, such as peripheral arterial occlusive disease (PAOD). However, not all patients have a native collateral circulation, and animal models suggest a genetic basis for this variability. In mice, such as the BALB/c, that lack native arteriolar collaterals, neocollateral formation from capillaries that connect two arterial trees can occur after arterial occlusion, resulting in reperfusion of the ischemic watershed. Immature arterialized collateral capillaries (ACCs) at 7 days post arterial occlusion do not vasodilate in response to physiological stimuli and are therefore unable to match blood flow with metabolic demand, but mature ACCs at 21 days exhibit normal vascular reactivity. Therefore we wanted to determine if vasodilation of ACCs at 21 days post arterial occlusion is capable of increasing flow throughout the ischemic arteriolar tree, because the ACCs are small-caliber vessels feeding progressively larger arterioles. One aspect of blood flow, vessel diameter, is measured routinely in our lab using bright field intravital microscopy; however blood velocity is more challenging to measure in the spinotrapezius microvasculature. In particular, we wanted to assess vasculature-wide changes in blood flow, which cannot be accomplished using laser Doppler flowmetry due to its small field of view or particle image velocimetry due to the curvature of the spinotrapezius. Therefore, we adapted a laser speckle flowmetry (LSF) protocol to measure blood velocity in the spinotrapezius microvasculature. In LSF, the scattering of laser light incident on the muscle produces a characteristic speckle. This speckle changes over time as erythrocytes flow through the vasculature of the muscle. If captured over the finite exposure time of a detector, the speckle is blurred, and the degree of blurring is related to the speed at which the erythrocytes are flowing through the vasculature. LSF yields velocity information across the entire field of view, and multiple fields of view can be stitched together to create a velocity map of the spinotrapezius vasculature. Using LSF, in conjunction with bright field intravital microscopy, we measured blood velocity and blood vessel diameter in vivo to quantify changes in blood flow. We found that vasodilation of mature ACCs (i.e. at day-21) increases blood flow (288 ± 72%) in the ischemic tree, which is comparable to the contralateral, control arterial tree (168 ± 76%), while vasodilation of immature ACCs (i.e. at day-7) does not increase blood flow (17 ± 27%) in the ischemic tree. The ability of mature ACCs to increase flow in the ischemic tree supports their potential as a therapeutic target for patients with PAOD who lack native collateral vessels. Future work will include the use of a contrast agent to provide more detailed vessel analysis (e.g. branch order effects), and similar analyses on mice with relevant comorbidities such as diabetes mellitus and hypercholesterolemia to study any potential impairment in arterialization and outward remodeling.

Keywords: collateral circulation, arteriogenesis, laser speckle flowmetry, laser speckle contrast imaging, peripheral arterial occlusive disease, ischemia

ACKNOWLEDGMENTS

Dr. Trevor Cardinal for his understanding, support, and guidance throughout this project. Protocol development has its high points and low points, but Dr. Cardinal was always there to support me.

My parents and grandparents for their unconditional support and willingness to listen to me ramble on for hours about this project. Without their sacrifices I would not have the opportunity to participate in this research.

My girlfriend for her patience and understanding throughout the past year. She kept me sane throughout many stressful days and nights.

Sara Hellstrom and Joshua Cutts for their patience in teaching me many of the lab techniques used in this project and for their contributions to the microcirculation and vascular regeneration lab.

The Hannah-Forbes fund for providing financial support for lab instruments that were used in this project.

"I hate cameras. They are so much more sure than I am about everything."
-John Steinbeck

Table of Contents

Contents

LIST OF FIGURES

LIST OF EQUATIONS

I. Introduction

Peripheral Arterial Occlusive Disease

Peripheral arterial occlusive disease (PAOD) is characterized by a buildup of atherosclerotic plaque in the arteries that supply blood to the peripheries of the body (**Figure 1**) as well as the head and organs [1]. This buildup of atherosclerotic plaque may occlude the vessel and limit the amount of blood supplied to the downstream tissues [1]. If left untreated, PAOD can lead to pain and numbness, impaired immunity, and eventual necrosis in the affected region [1].

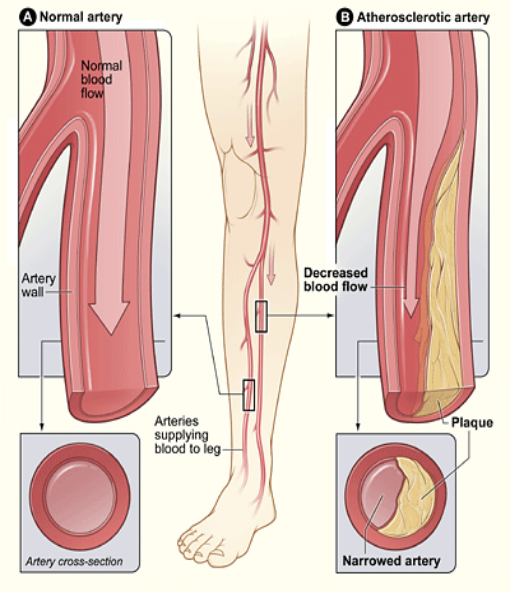

Figure 1. Atherosclerosis and Peripheral Arterial Occlusive Disease. Atherosclerosis in the arteries of the leg leads to ischemia (restriction of oxygen and nutrient-rich blood flow) in downstream tissues [1].

Globally, 202 million people were living with PAOD in 2010, and the prevalence of this disease is rising [2]. A number of treatment options currently exist depending upon the stage of the disease. Initial treatment entails modification of the major risk factors, which include smoking, hypertension, increased low-density lipoprotein levels, and diabetes mellitus. Pharmaceutical treatment such as a daily regimen of aspirin or another antithrombotic drug is often employed to reduce the risk of myocardial infarction and stroke. Intermittent claudication, or pain in the affected tissue region, is often the first

physical symptom to arise, and thus exercise therapy and pharmaceutical treatment are coupled to increase motility and function of the affected region.

If initial treatment does not reverse the development of the disease, surgical or percutaneous revascularization interventions are utilized. A major surgical intervention is bypass grafting whereby part of an autologous vein or a synthetic scaffold is used to make an artificial bypass around the occluded site [4]. A percutaneous intervention is angioplasty and stenting. This entails inserting a catheter with a balloon structure at the tip into the affected artery and inflating the balloon such that the plaque is pushed against the arterial wall and the site is left unobstructed. A stent (usually a cylindrical, metallic mesh structure) may ensheathe the balloon and thus may be deployed with the balloon dilation to keep the artery patent after the balloon is removed (**Figure 2**) [5]. Often, elderly patients are not good candidates for either of these treatments, and recurring adverse events such as restenosis and thrombosis may follow angioplasty and stenting. Thus there is a growing need for more effective, sustainable, and universal treatments for occlusive diseases such as PAOD.

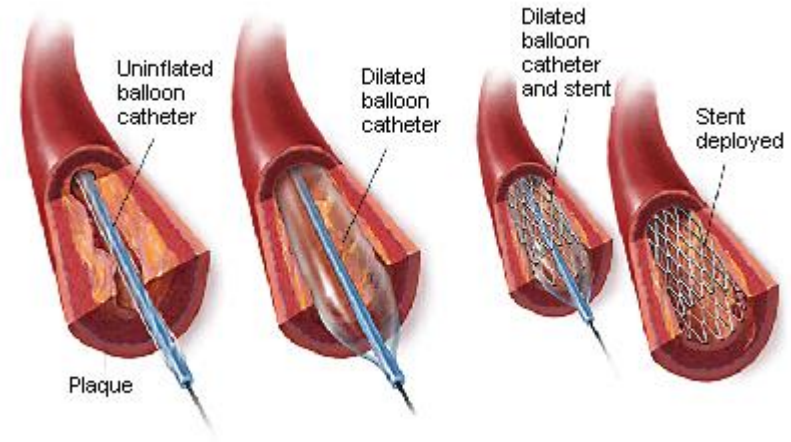

Figure 2. Endovascular Intervention. Angioplasty and stenting surgical treatment [3].

The Collateral Circulation

The surgical interventions described above have been practiced for over 50 years and still remain the standard for both coronary and peripheral occlusive disease treatment. However, some patients have a native collateral network of blood vessels, which consists of arterio-arteriolar anastomoses that can remodel to become functional bypass routes for blood flow around a site of occlusion (**Figure 3**) [6]. During occlusion, blood flow is diverted to the collateral vessels, thus increasing shear stress along the vascular walls of the collateral network. The increase in shear stress leads to collateral growth and outward remodeling, termed arteriogenesis [7, 8]. Ultimately, this response can produce a natural bypass network that can restore healthy function to the tissue downstream of the occlusion and thus improve prognosis for patients with PAOD [7].

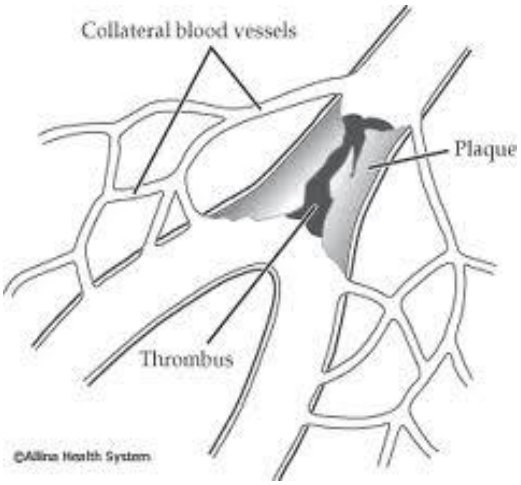

Figure 3. Collateral Blood Vessels. Collateral vessels can serve as natural bypass routes for blood flow around an occlusion.

Animal studies suggest a genetic basis for the extent of the native collateral circulation and show that collateral vessels form during embryonic development. Thus,

there is a large intra- and inter-species variability in the number and function of collateral vessels (**Figure 4**) [6].

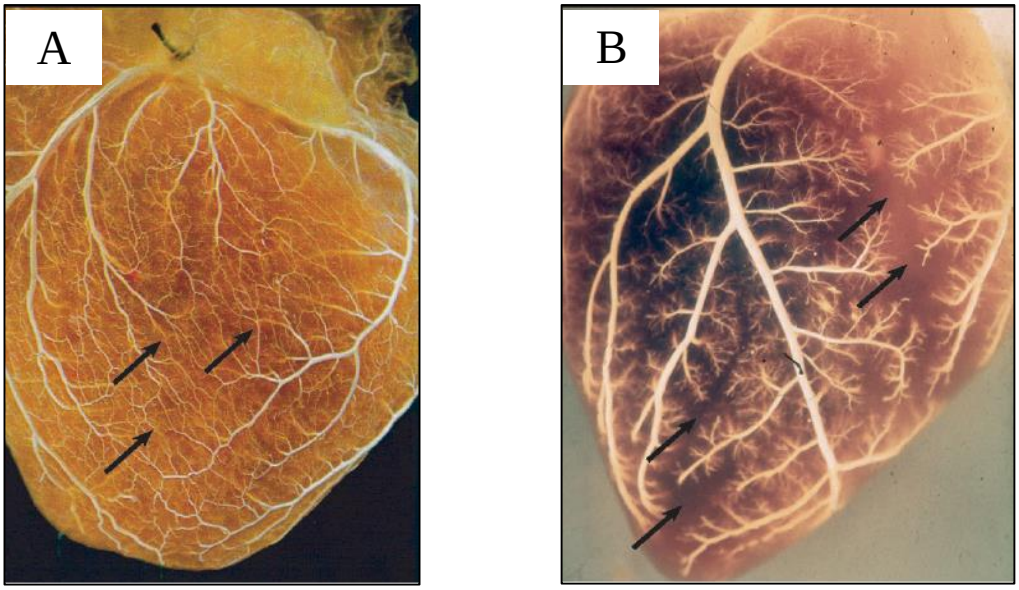

Figure 4. Variability in Collateral Networks. Genetic variability accounts for the whole spectrum of microcirculation, from many collateral vessels (A, canine coronary circulation) to no collateral vessels (B, porcine coronary circulation). Black arrowheads highlight the locations where arterioles either form collateral connections or terminate without forming collateral connections [9].

Animals lacking a native collateral circulation are more susceptible to ischemia, hypoxia (insufficient oxygen supply to the tissue), and eventual tissue necrosis following an occlusive event. In some animals that have no native collateral vessels, pre-existing capillary anastomoses that connect the ischemic arterial tree to a non-occluded arterial tree can become functional collateral vessels through a process known as collateral capillary arteriogenesis (CCA) [10]. The capillaries undergo a type of arteriogenesis known as arterialization, whereby they outwardly remodel and become invested with

smooth muscle cells, which may originate from upstream arterioles or may differentiate from mural pericytes [10]. Arterialization of capillaries may be initiated by a similar mechanism as arteriogenesis in collateral arterioles (i.e. increased fluid shear stress as a result of diverted blood flow through the capillaries), but the exact cellular mechanism is unknown.

Function of Arterialized Collateral Capillaries

Although ACCs appear to be an appealing alternative treatment option for patients with occlusive disease who lack a sufficient native collateral circulation, reperfusion of an ischemic region is not sufficient to restore function and eliminate physical symptoms. Equally important is the function and reactivity of the de novo collateral vessels. Vessels must respond to the dynamic physiological conditions of the downstream tissue by vasodilating and constricting in response to changes in metabolic demand. There are two facets of vasodilation and constriction: lumen diameter change and change in downstream blood flow. Both must occur for proper regulation of perfusion and maintenance of the tissue homeostasis.

During a period of increased metabolic activity such as running, the skeletal muscles involved require increased blood flow. The demand of the muscle is, at least in some part, communicated to the blood vessels by contraction of muscle fibers that lie underneath the capillary beds [11]. Hyperpolarization of arteriolar endothelial cells and the release of nitric oxide (NO) initiates the acute relaxation of smooth muscle cells and

local vasodilation in response to muscle contraction [12, 13, 14]. Local vasodilation ascends upstream to the larger arterioles and feed arteries, the dominant regulators of skeletal muscle resistance [13]. Since this cellular signaling is localized to the region of metabolic demand, only the vessels feeding the contracting muscle dilate.

Mature ACCs (21 days post occlusion) exhibit normal reactivity in terms of diameter increase in response to sodium nitroprusside (SNP), a smooth muscle cell-dependent vasodilator that is metabolized into NO, whereas immature ACCs (7 days post occlusion) do not exhibit normal reactivity [13]. However, the hemodynamics is not as straightforward as in the case with a normal microcirculation. In the majority of the microcirculation, blood flows from the feed artery to the arteriole tree and then to the capillary beds. Since blood flows from larger vessels down to smaller vessels, an increase in luminal diameter in the larger vessel leads to an increase in flow in the smaller vessels, given that the smaller vessels (capillaries) maintain a constant diameter. The ACCs, however, connect two arteriolar trees, and thus blood flows from a large vessel tree (non-occluded arteriole) to a small vessel and then into another large vessel tree (occluded arteriole) (**Figure 5**). In this case, blood flow in the occluded arteriole will not increase unless a sufficient number of ACCs feeds that arteriole. This is demonstrated by the Hagan-Poiseuille equation (Equation 1), where blood flow is inversely proportional to the radius of the vessel raised to the fourth power.

$$\text{Flow} \propto \Delta P = \frac{8\mu LQ}{\pi r^4} \quad (1)$$

Although an individual ACC is smaller in diameter than an arteriole, overall, the flow contributions of many ACCs may serve the same function as one arteriole. If the ACCs are capable of contributing an overall increase in flow during vasodilation then they may function as de novo collateral vessels, and thus may serve as a viable therapeutic target for patients lacking native collateral vessels.

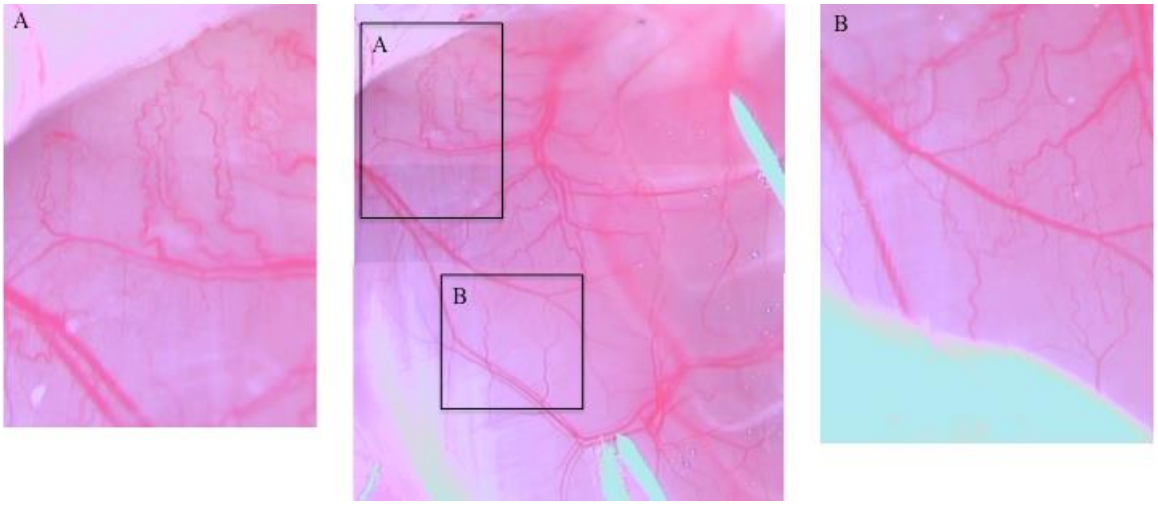

Figure 5. Arterialized Collateral Capillaries. In-vivo dissecting microscope image of ACCs in the Balb/c spinotrapezius connecting a cranial (A) and caudal (B) arteriolar tree to the ischemic tree.

State of the Art for Quantification of Blood Flow in Microcirculation

A method for measuring blood flow in the microcirculation is necessary to evaluate the ability of ACCs to increase flow in the ischemic tree following vasodilation. A number of methods exist for measuring blood flow in the microcirculation including sidestream dark field microscopy, intravital video microscopy, laser doppler flowmetry, and laser speckle flowmetry. The specific tissue preparation, anatomical constraints, and desired results play a major role in determining which imaging modality to employ.

Intravital Video Microscopy

Intravital video microscopy (IVVM) provides in vivo analysis of blood flow throughout a given vasculature, but requires a high-resolution camera and a flat preparation, usually achieved by using a window chamber. Recent studies utilize fluorescent tracers to measure blood velocity and vessel diameters in order to calculate blood flow. Fluorescent polystyrene microspheres or fluorescently marked erythrocytes may be injected into the circulation of the subject (**Figure 6**) [17]. Images captured using IVVM produce a streak line, showing the distance that the fluorescent tracer traveled during the exposure time of the image. Thus, the centerline streak length of the fluorescent tracer divided by the exposure time of the image gives an approximation for the centerline velocity, and flow may be calculated using the vessel diameter [17].

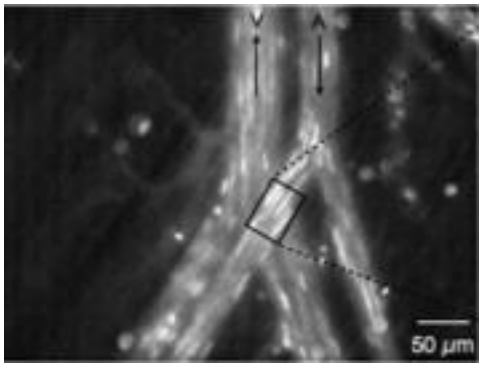

Figure 6. Intravital Video Microscopy. Fluorescently marked erythrocytes flowing through an artery/vein pair [17].

In order for IVVM to provide accurate data, the entire streak line of the tracer must be contained within the focal plane of the camera. This is difficult to achieve if the preparation is not completely flat because the focal plane is restricted by the slightest changes in depth. Although not reported with the fluorescently marked erythrocytes, microspheres may collect along the luminal walls of the vessels and extravasate into the

surrounding tissue. This impairs visualization of streak lines by producing significant background fluorescence.

Sidestream Dark Field Microscopy

Sidestream dark field (SDF) imaging is a common, non-invasive technique for measuring blood flow in the microcirculation. With this modality, concentric light emitting diodes (LEDs) positioned around the camera lens illuminate the vessels of interest [14]. Erythrocytes appear dark against the light tissue background because the LEDs emit a wavelength of light that is readily absorbed by hemoglobin but not by surrounding tissue or plasma (**Figure 7**) [14]. In many cases, this type of imaging allows for direct measurement of blood flow. SDF imaging is simple and portable, requiring a camera with a charge-coupled device (CCD) sensor connected to a computer for data storage and analysis [16]. However, artificial manipulation of blood flow in the region of interest can occur if the camera lens applies pressure to the vessel [16]. In general, since the camera lens must be in close proximity to the tissue, there is a substantial risk of contacting, and thus applying pressure to, the vessels. As another

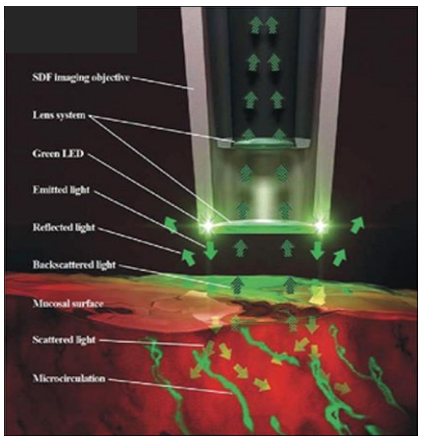

Figure 7. Sidestream Dark Field Imaging. Sidestream dark field imaging requires close contact of the lens with the tissue to illuminate and visualize blood flow [15].

consequence, SDF imaging cannot be used to image an entire arteriolar tree, but only one position along the tree because the lens may drag along the muscle and cause unintended damage. Additionally, it is difficult to obtain flow measurements in vessels where there is not a distinct contrast between the flowing erythrocytes and surrounding plasma, e.g. at high flow rates or in large vessels.

Laser Doppler Flowmetry

Laser Doppler flowmetry (LDF) uses the Doppler shift that occurs when light is reflected by moving objects to measure how fast blood cells are traveling [18]. LDF is a non-invasive procedure that can be performed transdermally when measuring flow in superficial vessels. The experimental setup for LDF is complex and expensive, involving a narrow band emission laser, optical fibers for transmitting and receiving light, a high frame rate camera, and analog/digital conversion of the signals to meaningful data [18]. LDF only provides flow information where the laser can directly illuminate, and thus cannot be used to analyze a vascular tree or a whole network.

Laser Speckle Flowmetry

Given the unique and still unknown hemodynamics of the collateral circulation, especially the arterialized collateral capillary network, the blood flow measurement method must yield whole arteriolar tree information while still providing accurate flow measurements. Laser speckle flowmetry (LSF) can be used to image an entire vascular network and, in conjunction with bright field imaging for diameter measurements,

provide flow information at any position along the network. Although similar to LDF, LSF takes advantage of a different phenomenon produced by the illumination of flowing erythrocytes with a laser.

A medium such as living tissue scatters light that is incident upon it. If the medium is static (i.e. there are no moving objects within it) then the scattering of light will be constant over time. If, however, there are moving objects such as cells within the medium, then the scattering of light will change as the objects travel through the medium. By capturing the resulting scatter pattern, or speckle, with a photodetector such as a charge-coupled device (CCD), the convective and diffusive movements of objects within the medium can be measured.

Laser speckle is produced by the random interference (both constructive and destructive) that occurs during the scattering of light by the medium. This random interference is caused by the unevenness of the scattering surface at the atomic level (**Figure 8**).

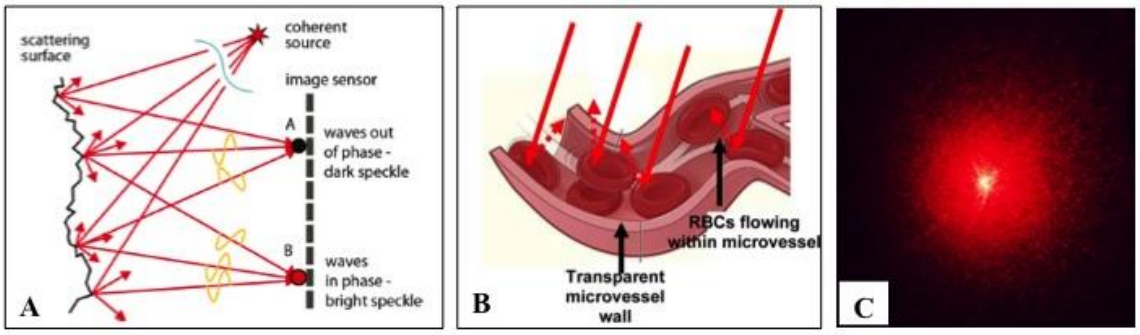

Figure 8. Laser Speckle Flowmetry. Coherent light incident upon a surface creates a speckle pattern. (A) The coherent light reflected off of a surface travels different path lengths to the image sensor as a result of the unevenness of the surface [19]. (B) When the surface is a blood vessel, there are moving objects (red

blood cells) within the vessel that cause uneven scattering [20]. (C) The differences in the path lengths cause constructive and destructive interference of the signal received by the image sensor resulting in areas of light and dark spots known as speckle [21].

Each element/pixel on the CCD registers a certain intensity of light that is dependent upon the random interference of light hitting the element at that moment. The CCD captures the change in the speckle pattern over time by collecting light over a given finite exposure time. As a result, the movement of the scattering objects blurs the final recorded speckle pattern [22]. That is, the pattern is fluctuating on a time scale smaller than the exposure time, and thus the CCD can only record an averaged result of all of the fluctuations that occurred during the exposure time [23]. However, this blurring effect is of practical use because the faster that the patterns fluctuate, the more blurred the final pattern will be.

Mathematically then, the blurring of the speckle pattern, and more specifically the contrast of the speckle pattern, can be related to the velocity of the moving object that is causing the speckle fluctuations. Assuming that the exposure time is constant, higher velocity causes a decrease in speckle contrast, due to blurring of the speckle, and lower velocity causes an increase in speckle contrast up to a theoretical maximum corresponding to the static medium case, also known as a "fully developed speckle pattern [24]." Since the measurement is with respect to a change in contrast, absolute velocity cannot be determined from LSF, only changes in velocity.

Laser Speckle Contrast Analysis Theory

The contrast value of each pixel is the most important piece of datum in LSF. There are a number of ways to determine the velocity of a scattering object based on the contrast of the images, however laser speckle contrast analysis (LASCA) is one of the first to be developed and one of the most simple to implement. LASCA uses the spatial variations in contrast for each image rather than the temporal variations in contrast over a stack of images to determine relative velocities. In LASCA, the contrast is calculated by using a 7 x 7 or 5 x 5 window of pixels around each pixel (**Figure 9**).

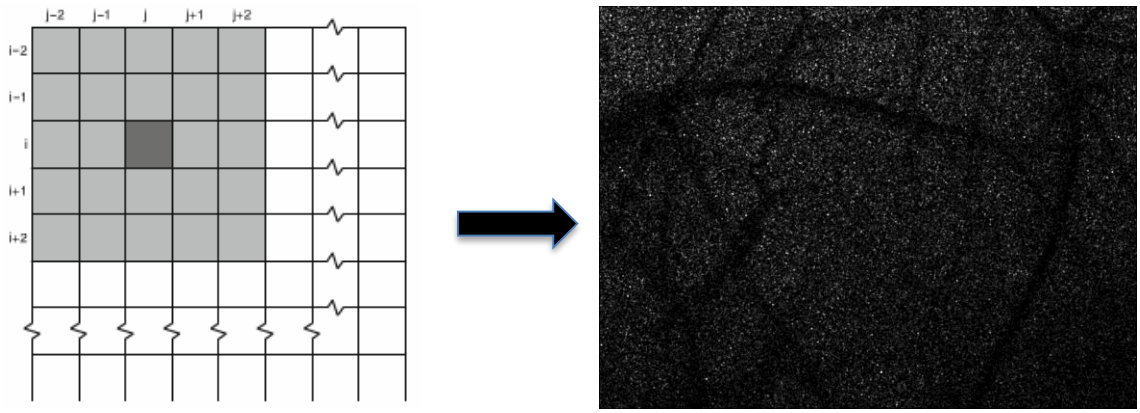

Figure 9. LASCA Computation Diagram. A sliding window of pixels is used to calculate the contrast value of each pixel. The contrast value is assigned a color along a grayscale. The resulting contrast map provides easy visualization of regions of high/low flow.

The contrast, C, of a given pixel at location (i,j) is given by the standard deviation of the pixel intensities over the mean pixel intensity of the 7 x 7 window, as shown in equation 1 [25, 26].

$$C_{ij}^2 = \frac{\sigma_{ij}^{7x7^2}}{(I_{ij}^{7x7})^2} \quad (2)$$

The contrast is directly related to the autocorrelation of the speckle, τ, which is a measure of how similar the speckle is over time. Thus, if the speckle changes dramatically over time, for example as a result of scattering objects moving quickly through the field of view, then the autocorrelation of the speckle will be low. If the speckle does not change over time, then the autocorrelation of the speckle will be high. Equation 2 shows that the contrast is directly related to the autocorrelation by a factor of the exposure time, T, and is inversely related to the speckle intensity, SI [25, 26].

$$\frac{1}{\tau} = \frac{1}{2TC^2} = SI \quad (3)$$

The SI is used to create a "map" of the blood velocity throughout the entire vasculature. Velocity maps are a simple way to compare individual vessel velocities as well as entire network velocities.

Specific Aims

Specific Aim 1: To create a protocol to use laser speckle flowmetry to quantify the change in flow in the feed arteriolar tree of the spinotrapezius muscle following vasodilation.

Specific Aim 2: To test the hypothesis that arterialized collateral capillaries can increase flow in the ischemic arterial tree at 21-days following ligation of the spinotrapezius muscle lateral feed artery to a comparable extent as the sham-operated.

Specific Aim 3: To test the hypothesis that arterialized collateral capillaries cannot increase flow in the ischemic arterial tree at 7-days following ligation of the spinotrapezius muscle lateral feed artery to a comparable extent as the sham-operated.

II. Methods

Animal Care and Housing

Male Balb/c mice were housed in microisolator cages (no more than four mice per cage) at the Cal Poly State University Vivarium, in temperature controlled (73 ± 5°F) rooms on a 12 hour light and dark cycle. The Balb/c mice were provided with unlimited food and water, and enrichment (contained nesting material, a plastic house, and a plastic tube). The mice were cared for and utilized under a protocol approved by the Cal Poly State University SLO Institutional Animal Care and Use Committee.

Spinotrapezius Ligation Surgery

The cranial, lateral feed artery of the spinotrapezius muscle was ligated and a sham operation was performed on the contralateral muscle in a Balb/c mouse, as previously described in [27] (**Figure 10**). Briefly, a small incision was made over the cranial, lateral aspect of the spinotrapezius muscle. Overlying fascia and connective tissue underneath the cranial fat pad was blunt dissected away to reveal the fat pad underneath the muscle. This fat pad was blunt dissected away from the muscle to expose the feed artery/vein pair. The artery was separated from the vein and two silk sutures were passed underneath the artery. The upstream suture was tied first, and then the downstream suture, and the artery was cut in between the two sutures. The fat pad was moved back into place and the incision was sutured closed. The sham operation was identical, but did not include the silk suture components.

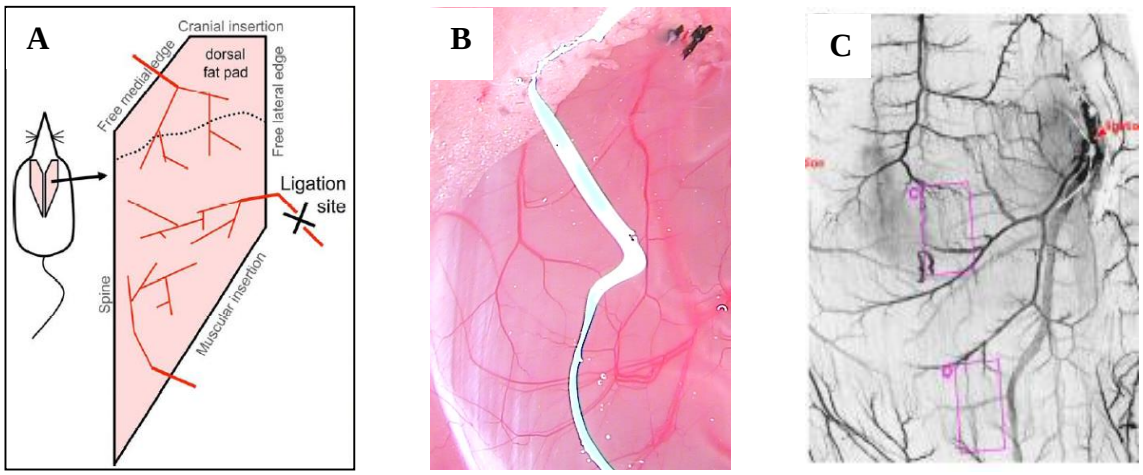

Figure 10. Spinotrapezius Feed Artery Ligation. Spinotrapezius feed artery ligation surgery: (A) general diagram [10] (B) in vivo ligation indicated by black sutures (C) smooth muscle actin stain with red arrow indicating ligation site and purple boxes indicating cranial and caudal regions of arterialized collateral capillary formation [10].

Mouse Preparation

In un-operated animals, and at days 7 and 21 following ligation of the cranial, lateral spinotrapezius feed artery, mice were induced using isoflurane gas (initially 5% flowing at 0.8ml·min^{-1}, and then maintained at 1-2% in oxygen flow at 0.8 – 1.2ml·min^{-1} for the duration of the procedure), and hair was removed from the dorsal aspect of the mouse with trimming clippers and depilatory cream. The mouse was then transferred to the surgical stage and a rectal thermistor probe was applied to provide feedback to a heat-pad system that maintained the mouse's core temperature at 35°C. An initial incision was made above the lateral edge of the spinotrapezius muscle, followed by blunt dissection of the underlying connective tissue, and further extension of the incision to reflect the skin

and expose the spinotrapezius muscle. The remaining superficial fascia on the muscle was removed to ensure maximum image quality.

Once exposed, a physiological salt solution (PSS) was irrigated over the preparation for the entirety of the imaging process to emulate the natural, in vivo environment of the muscle. PSS consisting of (in mM) 131.9 NaCl, 4.7 KCl, 1.17 $MgSO_4$, 2 $CaCl_2$, and 18 $NaHCO_3$ was heated to 35°C, bubbled with a 95%N_2/5%CO_2 gas mixture (to deoxygenate it), and flowed over the exposed spinotrapezius muscle at ~2ml·min^{-1}. The exposed spinotrapezius muscle was given 30 minutes after preparation described above to equilibrate before laser speckle imaging.

Once the vessels equilibrated (reached a stable resting diameter) the baseline flow measurements were made. The preparation was illuminated with an evenly distributed laser beam from a 40mW Coherent Cube laser set to 30mW output power with an expanding lens and mirror. An Olympus microscope with a 5X Olympus objective was centered above the muscle capture images with a QImaging Retiga EXi camera mounted to the microscope and connected to a computer via firewire cable. The QImaging QCapture Pro 7 software was used for image acquisition. All laser speckle images were captured with a 5ms exposure, a gain of 1, and as a stack of 60 continuous images. All overhead lighting was turned off during imaging. Dual fiber optic goosenecks connected to a halogen lamp were used for bright field images. **Figure 11** shows the experimental setup.

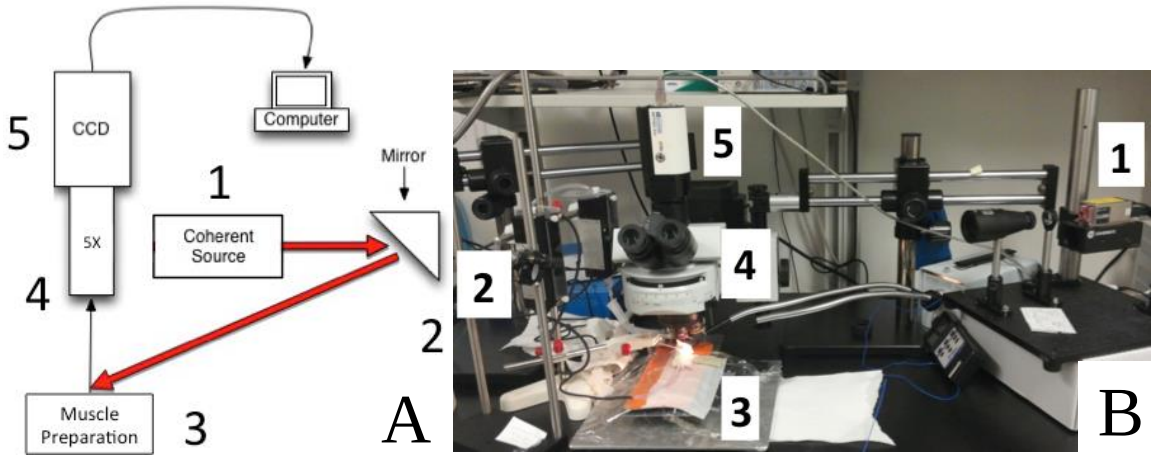

Figure 11. Laser Speckle Flowmetry Experimental Setup. Diagram (A) and experimental setup (B) showing the progression of imaging (larger image in appendix): 1. LED laser emits beam through expanding lens. 2. Beam is reflected by mirror. 3. Reflected beam illuminates exposed spinotrapezius muscle, which is superfused with PSS. 4. Resulting speckle pattern is collected by Olympus microscope. 5. Raw data is collected by QImaging CCD camera. Image on right adapted from [24].

Bright field and laser speckle images were captured across the entire spinotrapezius muscle. The brightfield images were used to ensure that the muscle was in focus as well as to take vessel diameter measurements. Thus, at each position across the muscle, a bright field image was captured before the laser speckle image. Once the baseline images were captured, sodium nitroprusside (SNP) at a stock concentration of 10^{-3} M, was added to 60mL of PSS to achieve the desired concentration (10^{-7}, 10^{-6}, 10^{-5}, or 10^{-4} M). The 60mL PSS and SNP solution was irrigated over the preparation for 5 minutes. Bright field and laser speckle images were captured across the spinotrapezius muscle in a similar manner such that the entire muscle was imaged after SNP application. For the dosage response experiment, each consecutive dose was followed by a 30 minute

resting period and proceeded from the lowest concentration (10^{-7} M) to the highest concentration (10^{-4} M). This process was completed on both muscles for the unoperated groups, and on the ligated muscle and then on the sham-operated muscle for day 7 and day 21 groups.

Following completion of the imaging for the day 7 and day 21 groups, both muscles were fixed in situ by irrigation with 4% paraformaldehyde for 15 minutes, and resected. The muscles were post-fixed in 4% paraformaldehyde overnight before rinsing and storing in phosphate-buffered saline. After resection, the mouse was euthanized by cervical dislocation. Resected muscles were stained for α-smooth muscle actin, mounted, and imaged using fluorescent microscopy. These images were used to guide the following analysis of the laser speckle and bright field images to ensure that collateral capillary arteriogenesis had occurred, and that the correct arteriolar trees were analyzed.

Image Processing and Measurements

Each laser speckle image stack was processed and reduced to one final contrast map using ImageJ and algorithms that employed the laser speckle contrast analysis theory previously presented (**Figure 9**). The first algorithm calculated the contrast for each pixel by using a 7 x 7 window (equation 1). The second algorithm removed out-of-focus images that were caused by the mouse's ventilation. Briefly, the mode pixel values of 5 randomly selected circular regions of background tissue were recorded for every image in a stack of contrast images and any image with more than 2 of those values reaching the

maximum possible pixel value (65535) was considered out-of-focus and removed from the stack. This algorithm was tested on numerous sets of contrast images and the resulting stacks were compared to manual removal of out-of-focus images to ensure that the algorithm produced consistent results. The final algorithm created an array that stored the median pixel value of each image in the contrast stack, calculated the median value of that array, subtracted from each individual image the difference between the overall array median and the individual image median, and then averaged all of the images in the stack together into one final image. Thus, each 60-image sequence was reduced to one final image from which laser speckle intensity (LSI) measurements were taken.

Velocity measurements were made by calculating the normalized speckle intensity (NSI) using equation 4 [26]. The LSI was calculated in ImageJ by using the line tool and recording the mean pixel intensity along the length of a given vessel or background tissue (**Figure 12**). Each vessel measurement was paired with its own adjacent background tissue measurement, and the length of the line used to measure both regions was kept constant so as to ensure that the mean was not biased by the size of the sample set.

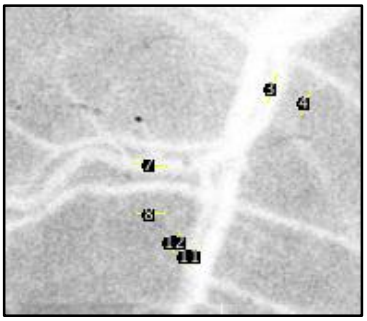

Figure 12. LSI Measurement. The ImageJ line tool was used to calculate mean pixel intensity (LSI) along the vessel and background tissue.

$$\mathrm{NSI} = \frac{\mathrm{LSI}_{\mathrm{vessel}}}{\mathrm{LSI}_{\mathrm{background}}} - 1 \qquad (4)$$

The line tool in ImageJ was used to measure vessel diameters in the corresponding bright field images. An approximation for the blood flow in a given vessel was calculated using equation 5 [26].

$$\text{Flow} \propto \text{NSI} * \pi\, r_{\text{vessel}}^2 \qquad (5)$$

All percent changes were calculated by comparing the SNP-treated vessel measurements to the baseline vessel measurements. Statistical analysis was performed using t-tests. Results are presented as mean ± standard error.

III. Results

In order to use laser speckle flowmetry (LSF) to assess arterialized collateral capillary (ACC) function, we first determined if we could use LSF to detect different degrees of blood flow changes by performing a sodium nitroprusside (SNP) dosage response experiment in unoperated mice. Arterioles exhibited peak vasodilation at 10^{-5} M SNP and the percent change in blood flow trended toward a similar behavior **(Figure 13)**.

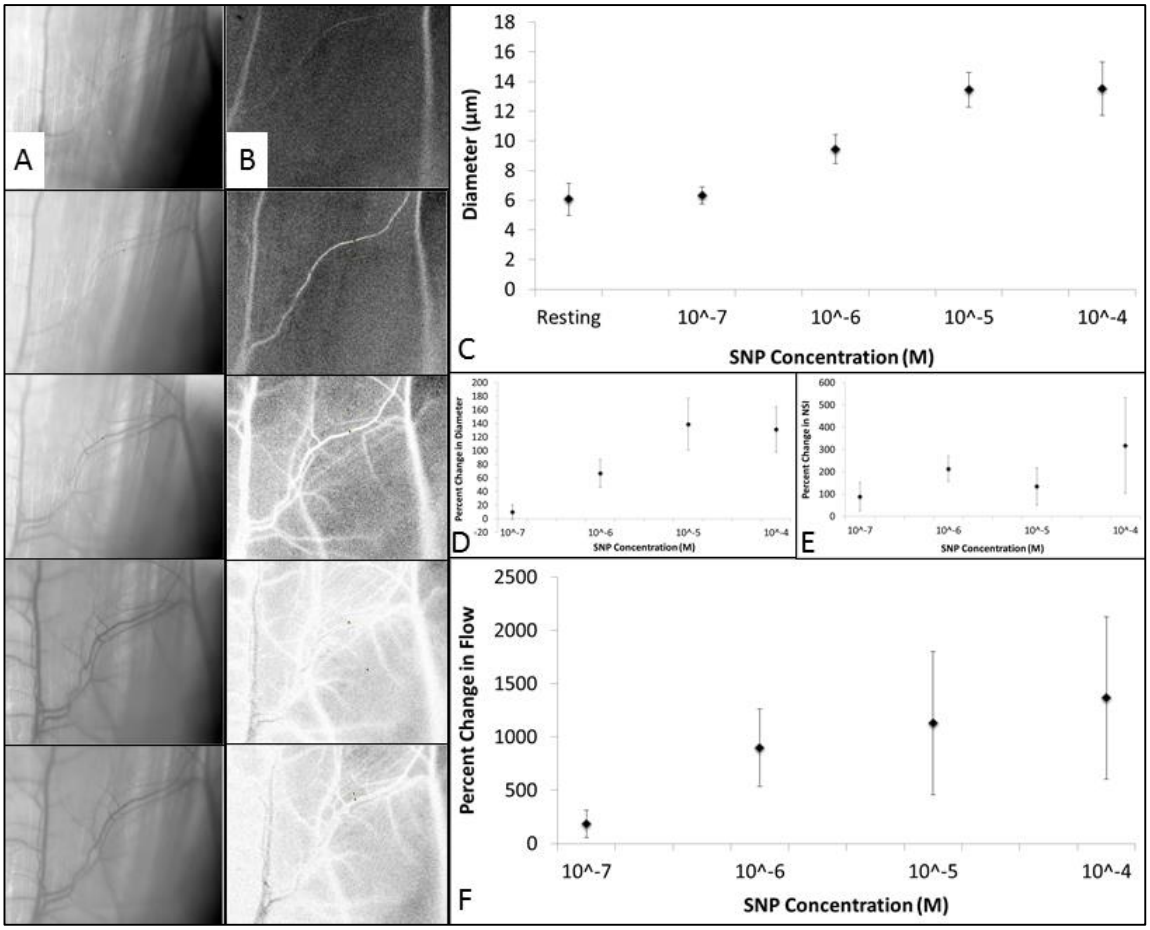

Figure 13. Laser Speckle Flowmetry (LSF) Dosage Response. (A and B) Representative bright field and laser speckle contrast images, respectively, showing arteriolar reactivity with increasing SNP concentrations from top (resting) to bottom (10^{-4} M). (C) Absolute arteriolar diameter at resting and after application of each SNP concentration showing no reactivity at 10^{-7} M and maximal reactivity at 10^{-5} M. (D) Percent change in arteriolar diameter after application of each SNP concentration showing consistent

behavior with absolute diameters. (E) Percent change in normalized speckle intensity (NSI) showing little change in blood velocity across the various concentrations. (F) Percent change in arteriolar blood flow showing a similar trend to the diameter changes (D), but with large variability. All data represent 2 different spinotrapezius muscles with a total of 5 different arterioles measured.

After assessing the sensitivity of LSF to changes in blood flow, we investigated the hypothesis that vasodilation of mature (i.e. day 21) ACCs increases blood flow in the ischemic tree comparable to sham, while vasodilation of immature (i.e. day 7) ACCs does not increase blood flow in the ischemic tree to a comparable extent. Vasodilation of mature ACCs increases blood flow (288 ± 72%) in the ischemic tree, which is comparable to the contralateral, control arterial tree (168 ± 76%), while vasodilation of immature ACCs (i.e. at day-7) does not increase blood flow (17 ± 27%) in the ischemic tree **(Figure 14)**.

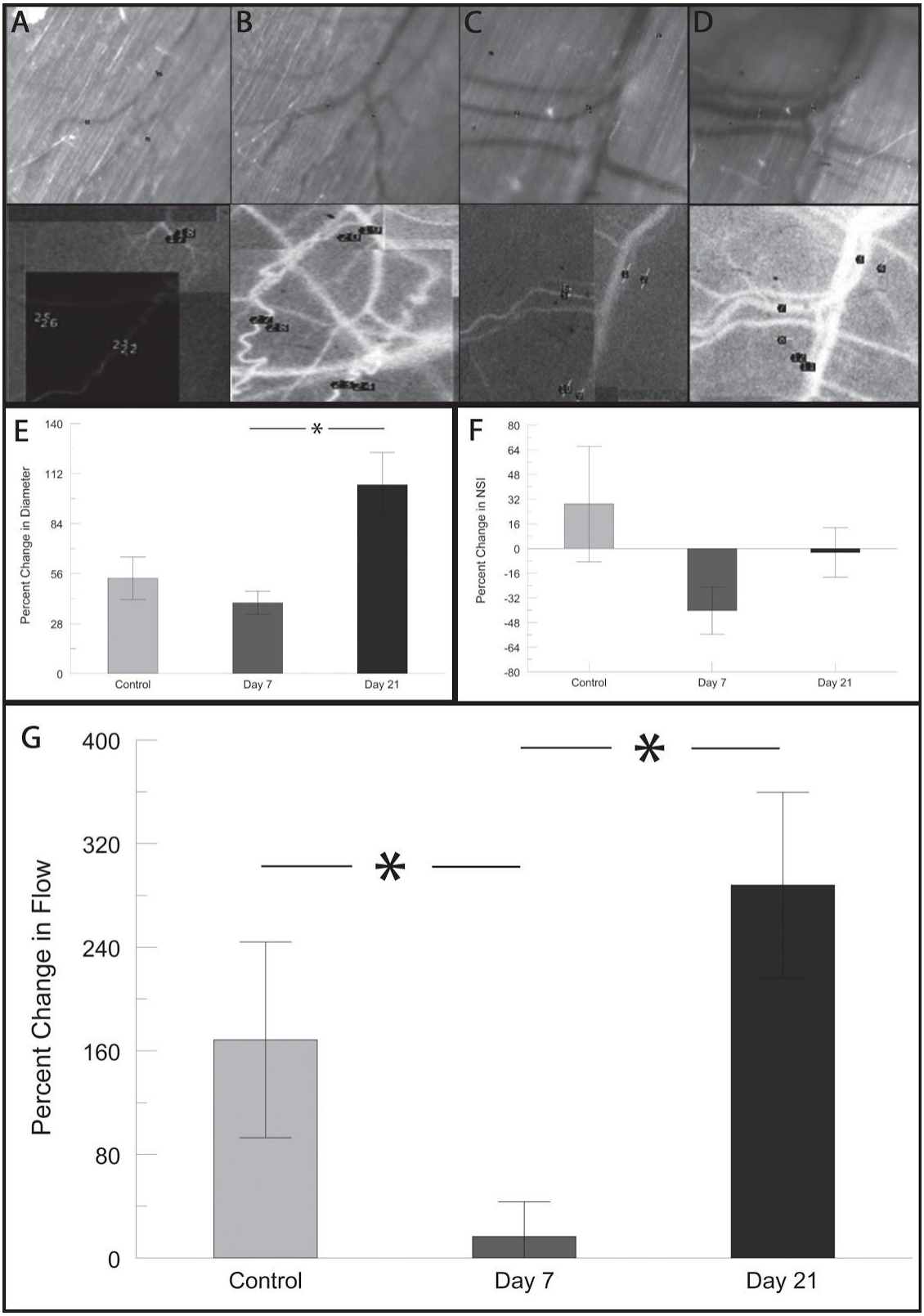

Figure 14. Vasodilation of Day-21 Arterialized Collateral Capillaries (ACCs) Increases Blood Flow in the Ischemic Tree. (A-D) Representative diameter measurements (top row) and laser speckle intensity

(LSI) measurements (bottom row), using the line tool in ImageJ. Note that each vessel LSI measurement is paired with an adjacent background LSI measurement. (E) Changes in vessel diameters throughout ischemic arteriolar tree after application of sodium nitroprusside (SNP) show greater increases in day 21 post-ligation group (n=5) than sham-operated group (control, n=5), as well as greater increases in day 21 post-ligation group (n=5) than day 7 post-ligation group (n=3). (F) Changes in blood velocity throughout ischemic arteriolar tree after application of SNP show no differences amongst sham-operated (control, n=5), day 21 post-ligation (n=5), and day 7 post-ligation groups (n=3). (G) Changes in flow throughout ischemic arteriolar tree after application of SNP show comparable percent increases in sham-operated (control, n=5) and day 21 post-ligation groups (n=5), but an impaired increase at day 7 (n=3). * denotes $p < 0.05$.

IV. Discussion

Peripheral arterial occlusive disease (PAOD) is characterized by the build up of atherosclerotic plaque in arteries supplying blood to the peripheries. This build up leads to ischemia in the downstream tissues and eventually tissue necrosis in the absence of clinical treatment. Current treatments such as bypass grafting and stenting are not suitable for all patients and suffer from limitations such as restenosis. Interestingly, some patients possess native collateral circulations that provide natural bypasses for blood flow around an occlusion. The presence of native collateral circulations improves prognosis for patients with ischemic disease [28]. In animals such as the Balb/c mice that generally lack native collateral arterioles, collateral capillaries connecting two arteriole trees undergo collateral capillary arteriogenesis (CCA) in response to an occlusion, eventually becoming functional collaterals [10]. Once mature, these new arterialized collateral capillaries (ACCs) exhibit phenotypic behavior of normal arterioles: vasodilating and constricting in response to chemical signals and expressing alpha smooth muscle actin [10, 13].

However, the ACCs are smaller in diameter than normal pre-existing collateral arterioles (appendix A). Thus, although the CCA may restore perfusion to the ischemic region, it is not known whether the vasodilation of the ACCs can cause an increase in flow in the ischemic tree. In a physiological state, metabolic stress such as exercise would require the dilation of arterioles to increase blood flow to downstream tissues. To maximize the efficacy of CCA as a therapeutic target for patients with ischemic diseases, such as peripheral arterial occlusive disease (PAOD), the newly formed collaterals would have to regulate flow to meet the metabolic demands of downstream tissue.

In order to assess ACC regulation of blood flow, we adapted a laser speckle flowmetry (LSF) protocol from [26] to measure blood flow in the Balb/c spinotrapezius microcirculation. We first established the accuracy and sensitivity of the imaging system by performing a dosage response study in unoperated Balb/c mice. We used data from previous dosage response studies performed in our lab to validate the LSF results. The vessel diameters are consistent with previous dosage response studies, however the blood velocity, which is proportional to the normalized laser speckle intensity (NSI), does not change across the various vasodilator concentrations (**Figure 13)**. Additionally, the NSI data exhibit significant variability, which translates to variability in the overall blood flow data. Although the flow trends toward similar behavior to the vessel diameter, the variability obscures the sensitivity of LSF. The dosage response study suffered from a low number of replicates, however additional explanations for the variability are discussed further in the limitations.

We then used the LSF protocol to assess the effect of ACC vasodilation on blood flow in the ischemic tree in Balb/c following spinotrapezius feed artery ligation. The results supported the hypothesis that, during vasodilation, mature ACCs (21 days post-ligation) increase flow to the ischemic tree to a comparable extent as healthy arterioles, and immature ACCs (7 days post-ligation) exhibit an impaired ability to increase flow (**Figure 14**). These results are in agreement with previous studies showing that mature ACCs are reactive in terms of diameter increases to physiological vasodilators such as sodium nitroprusside (SNP) and muscle contraction, and that immature ACCs exhibit impaired reactivity [13, 29]. The study presented here supports the role of ACCs as a

possible therapeutic option for patients with PAOD who lack a sufficient native collateral circulation.

Limitations and Future Work

LSF suffers from a number of limitations including uniform illumination of the muscle and resolution of the speckle and bright field images. The spinotrapezius muscle is located next to the spine of the mouse and thus has a natural pronounced curvature. This makes it difficult to uniformly illuminate the muscle with an expanded laser beam because each portion of the muscle lies at a different angle in relation to the beam. As a result, certain portions of the muscle are more uniformly illuminated than others, producing some images that have higher background intensities than others. Normalizing each vessel intensity to the adjacent background intensity reduces this bias, but the data may suffer from non-uniformity.

The ventilation of the mouse also introduces inconsistency in the speckle images. During image acquisition, the mouse may breathe 3 or 4 times, and thus a number of the images in the stack are out of focus because the muscle is elevated out of the focal plane of the microscope at the peak of the ventilation cycle. Previously, the observer manually removed the out-of-focus images before averaging the image stack. This is somewhat subjective because an out-of-focus speckle image is not as easily identified as an out-of-focus bright field image. Using ImageJ, we created a macro to automatically sort out the undesired images based on a pixel intensity analysis in order to further standardize the image processing and remove any subjectivity.

The sorting macro proceeded as follows: the mode pixel value of 5 randomly selected circular regions of background tissue were recorded for every image in a stack of

contrast images, and any image with more than 2 of those values reaching the maximum possible pixel value (65535 for a 16-bit depth image) was considered out-of-focus and removed from the stack. The threshold pixel value was motivated by the observation that out-of-focus images were consistently brighter than in-focus images. We validated the accuracy of the algorithm by testing it on numerous sets of contrast images and comparing the results to manual removal of out-of-focus images.

Laser Speckle Resolution: Methods of Analysis

The resolution of laser speckle images is partly dependent upon the method of analysis (i.e. the domain from which the contrast of each pixel is calculated). Spatial laser speckle contrast analysis (sLASCA) uses a spatial domain to determine the contrast of a particular pixel, while temporal LASCA (tLASCA) uses a temporal domain [20]. The method used in this study is a form of sLASCA (using a 7x7 spatial window) that includes stack normalization, effectively averaging across a temporal domain to reduce a stack of images into one image. sLASCA returns poor spatial resolution while tLASCA returns poor temporal resolution since each method sacrifices data in the spatial or temporal domain, respectively [20]. Temporal resolution is not important in this study because we are only interested in measuring relative blood flow at two distinct time points (resting and dilated).

Some of the spatial resolution losses inherent in sLASCA are overcome by using larger stacks of images for each field of view because there is less chance for data to be lost during the final stack normalization. Automation of image analysis (e.g. by automating out-of-focus image removal) allows for acquisition of larger stacks of images at each position along the muscle because manual inspection of 60 images per stack is

cumbersome and inefficient. Nevertheless, tLASCA is better suited for this study because it provides better inherent spatial resolution. Spatio-temporal LASCA (stLASCA) may provide even better resolution because it uses both spatial and temporal domains, but sample results of these methods do not justify the longer computation time required to complete stLASCA versus tLASCA (**Figure 15**).

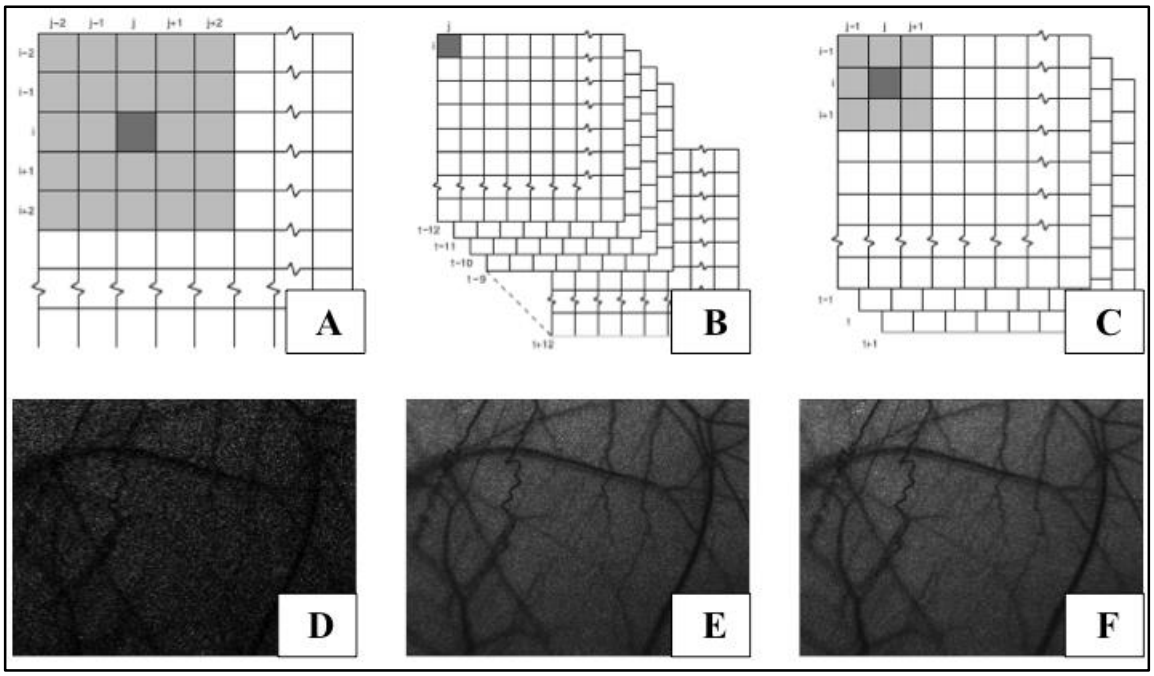

Figure 15. Laser Speckle Analysis Methods. Different laser speckle analysis methods result in differing spatial and temporal resolutions. (A) sLASCA calculates the contrast from the neighboring pixels in a spatial window around the pixel of interest. (B) tLASCA calculates the contrast from the same pixel across a number of images in a stack. (C) stLASCA calculates the contrast using a cube of pixels that extends in the spatial and temporal domains. (A-C) were adapted from [30]. (D-F) Corresponding results from the three methods of analysis using the same field of view, a 3x3 spatial window, and a 15 image temporal window show a marked difference in vessel visibility. These images are contrast maps, and thus are the inverse of the images shown in the results section. The three methods were implemented using Visual C++, and the code is included in the appendices.

Background Scattering

One unresolved issue that is particularly apparent in the dosage response study is the increase in background speckle intensity concomitant with increases in vessel speckle intensity. SNP concentrations of 10^{-5} M and 10^{-4} M exhibit the highest magnitude of background speckle intensity (**Figure 13)**. This rise in background signal is likely due to the effects of vasodilation since the imaging system is not modified once the dosage response experiment is started (i.e. the laser, camera, and mouse position do not change over the various dosages) and the rise is consistent amongst all replicates. It is possible that the high background signal is a result of increased capillary perfusion that cannot be resolved by the imaging system. In the case of cranial laser speckle imaging, one of the most common applications of LASCA, 95% of the speckle signal originates from the top 700μm of the tissue, with only 10% of parenchymal signal originating in the top 50μm [31]. Given that the spinotrapezius is only 50-200μm thick (depending upon the location along the muscle), it is also possible that vessels in the muscle underlying the spinotrapezius also contribute to the background signal [27]. Regardless of the origin of the signal, it is clear from the dosage response study that the background signal reaches a magnitude comparable to that of the vessel, and thus normalization to the background results in underestimation of the blood flow velocity at high SNP concentrations. Given that there is not yet consensus on how parenchymal regions should be processed differently from surface vessel regions, different normalization strategies should be utilized to more accurately estimate blood flow velocity [31].

Bright Field Resolution

The contrast analysis method affects the accuracy of blood velocity measurements, but the accuracy of the vessel diameter measurements is equally important for calculating blood flow. In this study, bright field imaging is used to assess vessel diameters, but this imaging modality suffers from the inability to resolve vessels as small as the terminal arterioles or ACCs because there is not sufficient contrast between the vessels and the background tissue. As a result, there were not enough replicates for each ordered vessel to provide a branch-order analysis of the flow data. Injection of a contrast agent such as a fluorescently labeled dextran into the mouse circulation provides better contrast, allowing for visualization of vessels at the terminal arteriole and capillary levels (**Figure 16**). The accuracy of vessel diameter measurements is dependent upon accurate discernment of the vessel walls. Thus, better contrast not only allows for visualization of smaller vessels, but, in general, provides more accurate diameter measurements.

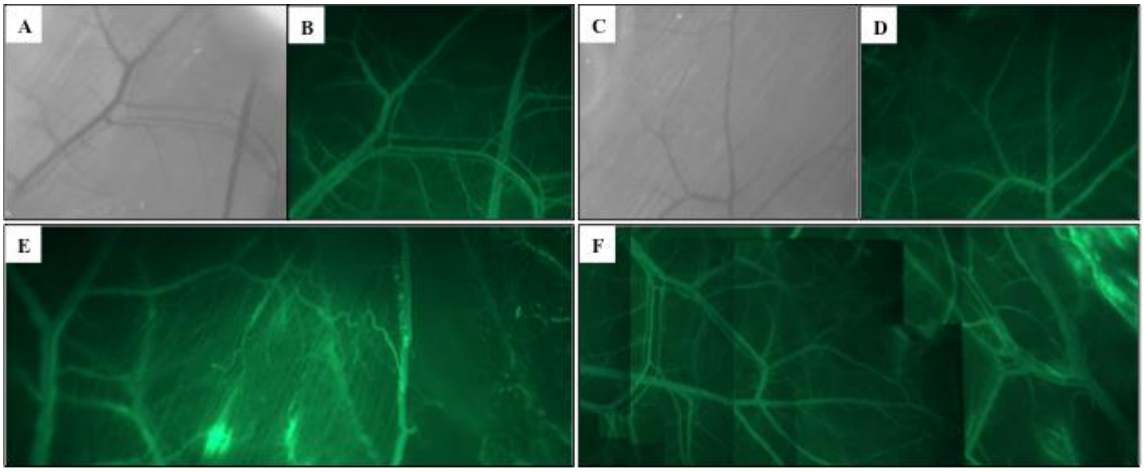

Figure 16. Fluorescent Contrast Agent for Vessel Visualization. Fluorescein isothiocyanate (FITC)-dextran injection provides better contrast for visualization of blood vessels in vivo (all images are 5X magnification). (A, C) Representative bright field images. (B, D) Representative fluorescent images of same fields of view in (A) and (C). (E) Terminal arterioles leading into capillary bed. (F) Photo montage of spinotrapezius vasculature using FITC-dextran as a contrast agent.

We completed initial testing of contrast agents for better vessel diameter measurements during the course of this study. FITC-dextran was used because it is relatively inexpensive and it provides capillary-level visualization in the spinotrapezius. Future work in this area will include the use of a jugular vein catheter to provide multiple injections of FITC-dextran throughout the duration of imaging. This is motivated by the observation that the FITC-dextran photobleaches during the 6-8 hour-long imaging procedure.

Immediate future work will integrate FITC-dextran and improved laser speckle image analysis to complete the analysis of regional and branch order effects on blood flow. Preliminary speckle intensity data organized based on region (cranial versus caudal) and branch order are presented in appendices C and D, respectively, however there are not sufficient diameter measurements to calculate flow data for these categories.

Regional Hemodynamics

The imaging processes may not be the only factor in assessing blood flow because the region of interest may also affect the data. In the Balb/c spinotrapezius, ACCs form between the ischemic arteriole tree and the healthy arteriole trees surrounding it [10]. Most proximally to the ischemic tree ACCs form connections with one cranial tree and one caudal tree. Alpha smooth muscle actin stains of the muscle show that the ACCs connecting to the cranial tree are qualitatively larger than the ACCs connecting to the caudal tree, although perhaps not as numerous (appendix C). Although not specifically addressed in the study, representative isolectin/α-SMA images of the Balb/c spinotrapezius 3 days post-ligation from [32] also show a higher density of collateral capillaries in the cranial region than in the caudal region. Given that the ACCs outwardly

remodel in response to increased shear stress, it is possible that the larger diameters of the cranial ACCs at 21 days post-ligation indicate that this region of collateral capillaries receives more of the redirected flow immediately after occlusion [10]. The greater redirection of flow in the cranial region may lead to more evident rarefaction of the cranial ACCs, a process noted in [10] to occur at 14, 21, and 42 days post-ligation, between days 3 and 21, thus leading to larger diameters.

With the existence and function of ACCs in healthy mice established, the next step will be to study similar processes in mice with relevant comorbidities to atherosclerosis such as diabetes mellitus (DM) and hypercholesterolemia. These pathological states negatively affect collateral remodeling in a number of ways, which may translate to similar negative effects in collateral capillary arterialization and subsequent outward remodeling involved in CCA. Heightened inflammatory states in both DM and hypercholesterolemia may impair the recruitment of inflammatory cells such as monocytes/macrophages to the site of remodeling. In addition, both DM and hypercholesterolemia have negative effects on the bone marrow microenvironment, thus causing impairments in stem cells that potentially play a role in arteriogenesis [7]. Vascular endothelial growth factor (VEGF)-resistance is associated with hypercholesterolemia, and VEGF is a key player in arteriogenesis [33, 34]. Many cardiovascular pathologies are associated with the inability of small arteries to remodel over time, and thus the ability of ACCs to remodel is crucial to their therapeutic potential in arterial occlusive diseases [35].

References

1. U.S. Department of Health and Human Services. National Heart, Lung, and Blood Institute. “What Is Peripheral Arterial Disease?” 1 April 2011. Web. 11 December 2013.

2. Fowkes, F, Rudan, D, Rudan, I, Aboyans, V, Denenberg, J, McDermott, M, Norman, P, Sampson, U, Williams, L, Mensah G, Criqui, M. Comparison of global estimates of prevalence and risk factors for peripheral artery disease in 2000 and 2010: a systematic review and analysis. The Lancet 382:1392-1340, 2013.

3. Boston Scientific. Lifebeat. Angioplasty and Stent Implantation. Web. 5 June 2014.

4. Willigendael E, Teijink J, Bartelink M-L, Peters R, Büller H, Prins M. Smoking and the patency of lower extremity bypass grafts: A meta-analysis. Journal of Vascular Surgery 42: 6774, 2005.

5. U.S. Department of Health and Human Services. National Heart, Lung, and Blood Institute. “How Is Peripheral Arterial Disease Treated?” 1 April 2011. Web. 11 December 2013.

6. Wang S, Zhang H, Wiltshire T, Sealock R, Faber J. Genetic dissection of the Canq1 locus governing variation in extent of the collateral circulation. PloS one 7: e31910, 2012.

7. Silvestre J-S, Smadja D, Lévy B. Postischemic revascularization: from cellular and molecular mechanisms to clinical applications. Physiological reviews 93: 1743–802, 2013.

8. Schaper, W and Heil, M. Influence of mechanical, cellular, and molecular factors on collateral artery growth (arteriogenesis). Circulation Research 95: 449-458, 2004.

9. Heil, M, Eitenmüller, I, Schmitz-Rixen, T, and Schaper, W. Arteriogenesis versus angiogenesis: similarities and differences. Journal of Cellular and Molecular Medicine 10(1): 45-55, 2006.

10. MacGabhann F, Peirce S. Collateral capillary arterialization following arteriolar ligation in murine skeletal muscle. Microcirculation (New York, N.Y. : 1994) 17: 333–47, 2010.

11. Cohen, KD and Sarelius, IH. Muscle contraction under capillaries in hamster muscle induces arteriolar dilatation via K(ATP) channels and nitric oxide. The Journal of Physiology 539: 547-555, 2002.

12. Hellsten, Y and Clifford P. Vasodilatory mechanisms in contracting skeletal muscle. Journal of Applied Physiology 97: 393-403, 2004.

13. Segal, S, Heijden, B, Haug, S, With, M. Ischemia-reperfusion impairs ascending vasodilation in feed arteries of hamster skeletal muscle. Microcirculation 12: 551-561, 2005.

14. Murrant, CL, Duza, T, Kim, MB, Cohen, KD, and Sarelius, IH. Arteriolar dilations induced by contraction of hamster cremaster muscle are dependent on changes in endothelial cell calcium. Acta Physiologica Scandinavica 180(3): 231-238, 2004.

15. Hellstrom, S. Vascular Reactivity of Immature Arterialized Collateral Capillaries. Senior Project. California Polytechnic State University, San Luis Obispo, Print.

16. Goedhart P, Khalilzada M, Bezemer R, Merza J, Ince C. Sidestream Dark Field (SDF) imaging: a novel stroboscopic LED ring-based imaging modality for clinical assessment of the microcirculation. Optics Express 15, 2007.

17. Gupta, P, Ashok, L, Naik, S. SDF imaging for assessing mucosal microcirculation and its correlation with OSMF. International Poster Journal of Dentistry and Oral Medicine 14:576, 2012.

18. Balestra G, Bezemer R, Boerma E, Yong Z-Y, Sjauw K, Engstrom A, Koopmans M, Ince C. Improvement of sidestream dark field imaging with an image acquisition stabilizer. BMC medical imaging 10: 15, 2010.

19. Al-Khazraji, B. A Simple ‘‘Streak Length Method’’ for Quantifying and Characterizing Red Blood Cell Velocity Profiles and Blood Flow in Rat Skeletal Muscle Arterioles. Microcirculation. (2012)

20. Swiontkowski, M. Laser Doppler Flowmetry – Development and Clinical Application. The Iowa Orthopaedic Journal.

21. Speckle Sense, MIT Media Lab.

22. Thakor, N, Li, N, Rege, A, and Senarathna, J. Laser Speckle Contrast Imaging: Theory, Instrumentation and Applications. IEEE Reviews in Biomedical Engineering 6: 99-110, 2013.

23. Shpyrko Research Group, UCSD.

24. Briers, J and Fercher, A. Flow visualization by means of single-exposure speckle photography. Optics Communications Volume 37, Number 5, 1981.

25. Webster, S and Briers, J. Laser speckle contrast analysis (LASCA): A nonscanning, full-field technique for monitoring capillary blood flow. Journal of Biomedical Optics 1: 174-179, 1996.

26. Meisner J, Sumer S, Murrell K, Higgins T, Price R. Laser speckle flowmetry method for measuring spatial and temporal hemodynamic alterations throughout large microvascular networks. Microcirculation (New York, N.Y. : 1994) 19: 619–31, 2012.

27. Guendel, AM, Martin, KS, Cutts, J, Foley, PL, Bailey, AM, Gabhann, FM, Cardinal, TR, and Peirce, SM. Murine spinotrapezius model to assess the impact of arteriolar ligation on microvascular function and remodeling. Journal of Visualized Experiments (73), e50218, 2013.

28. Regieli, JJ, Jukema, JW, Nathoe, HM, Zwinderman, AH, Ng, S, Grobbee, DE, van der Graaf, Y, and Doevendans, PA. Coronary collaterals improve prognosis in patients with ischemic heart disease. International Journal of Cardiology 132: 257-262, 2009.

29. Cutts, Josh, Feilim MacGabhann, and Trevor Cardinal. "Functional Vasodilation of Arterialized Capillaries Is Impaired in the Spinotrapezius." Senior Project. California Polytechnic State University San Luis Obispo, n.d. Print.

30. Draijer M, Hondebrink E, Leeuwen T, Steenbergen W. Review of laser speckle contrast techniques for visualizing tissue perfusion. Lasers in Medical Science 24: 639–51, 2009.

31. Davis, MA, Kazmi, SMS, and Dunn, AK. Imaging depth and multiple scattering in laser speckle contrast imaging. Journal of Biomedical Optics 19(8):086001, 2014.

32. Bruce AC and Peirce SM. Exogenous thrombin delivery promotes collateral capillary arterialization and tissue reperfusion in the murine spinotrapezius muscle ischemia model. Microcirculation 19: 143-154, 2012.

33. Waltenberger, J, Lange, J, and Kranz, A. Vascular endothelial growth factor-A-induced chemotaxis of monocytes is attenuated in patients with diabetes mellitus: a potential predictor for the individual capacity to develop collaterals. Circulation 102: 185-190, 2000.

34. Simons, M, Lanahan, A, Zhang, J, Zhuang, Z, Gabhann, F, Paye, J, and Moraes, F. Endothelial cell-dependent regulation of arteriogenesis. Circulation Research 113: 1076-1086, 2013.

35. Meininger, G, Hill, M, and Martinez-Lemus, L. The plastic nature of the vascular wall: a continuum of remodeling events contributing to control of arteriolar diameter and structure. Physiology 24: 45-57, 2008.

Appendix A

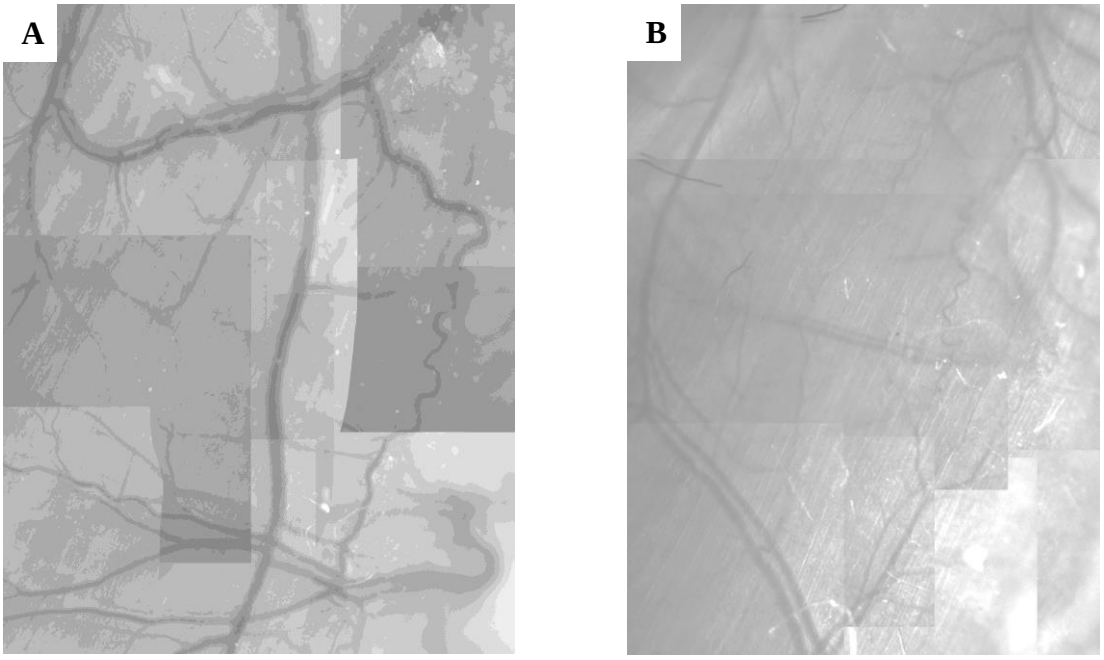

Figure 17. Sizes of Pre-existing Collaterals and Arterialized Collateral Capillaries. Brightfield images (5X magnification) showing the relative size of (A) pre-existing collaterals and (B) arterialized collateral capillaries in Balb/c spinotrapezius.

Appendix B

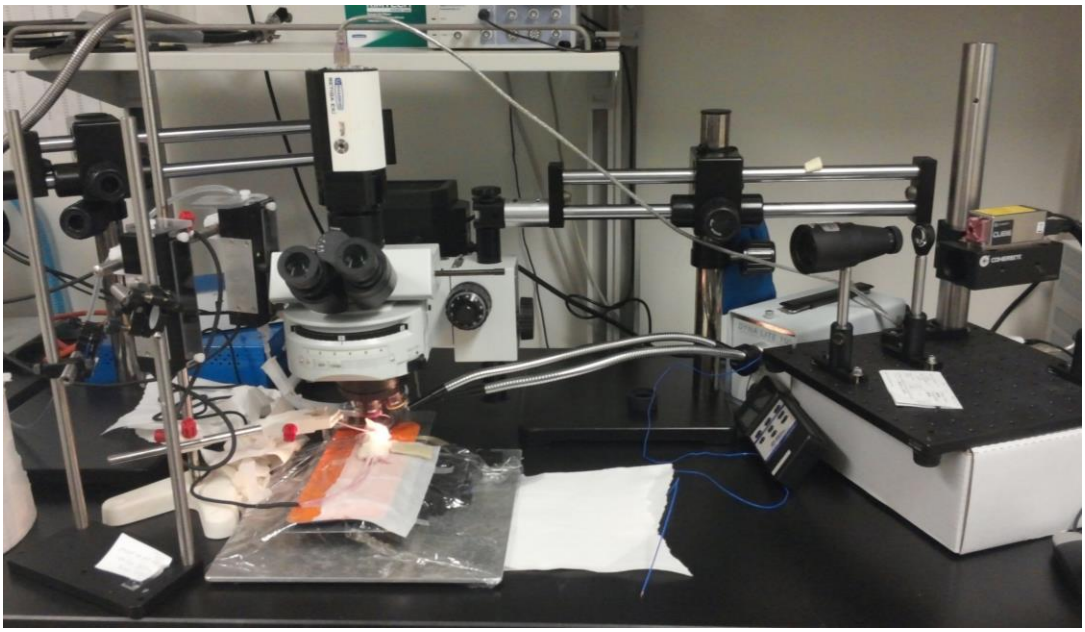

Figure 18. Laser Speckle Flowmetry Experimental Setup (Enlarged) Laser speckle flowmetry experimental setup (larger version of figure 10).

Appendix C

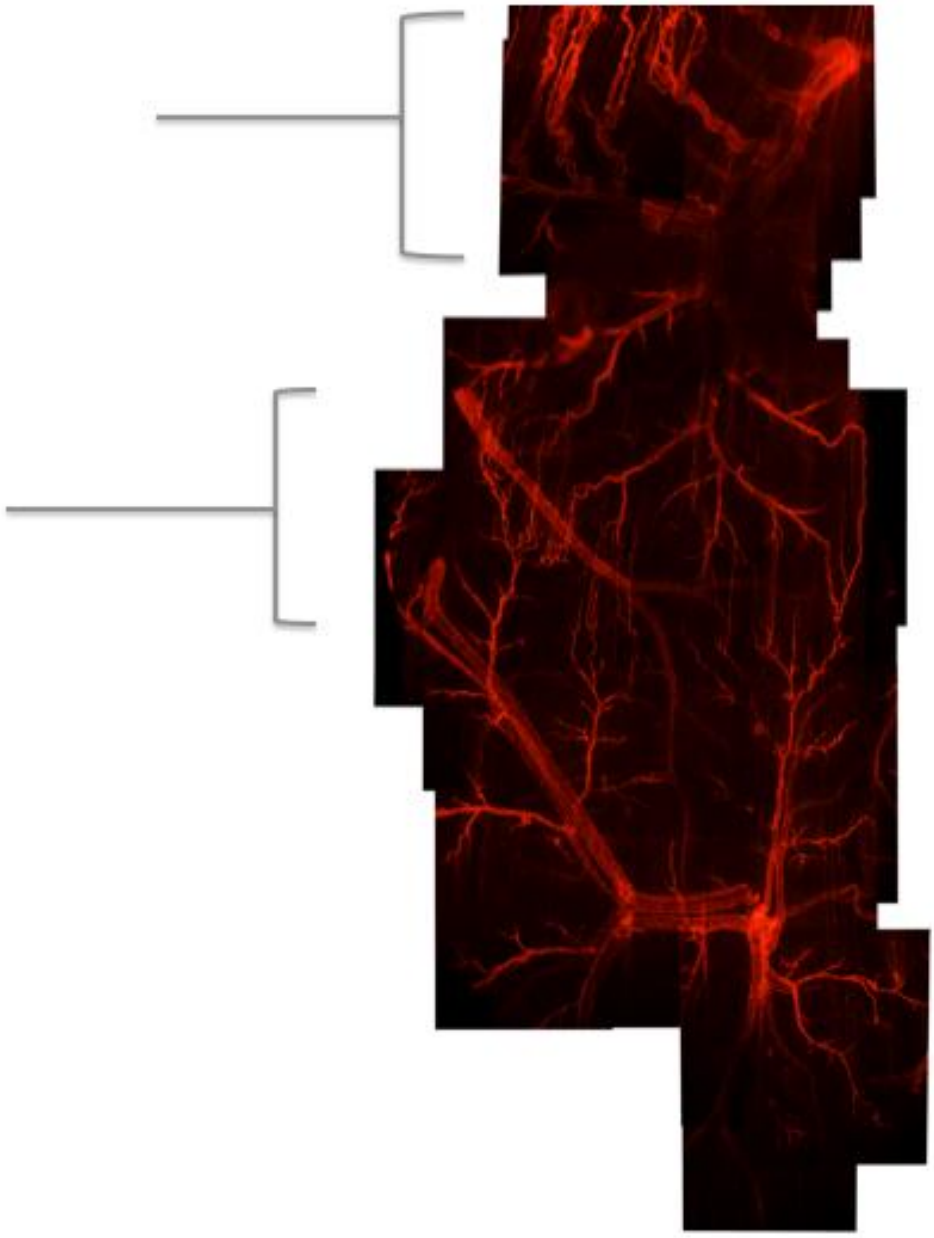

Figure 19. Cranial and caudal arterialized collateral capillaries. Arterialized collateral capillaries in the cranial (upper bracket) and caudal (lower bracket) regions.

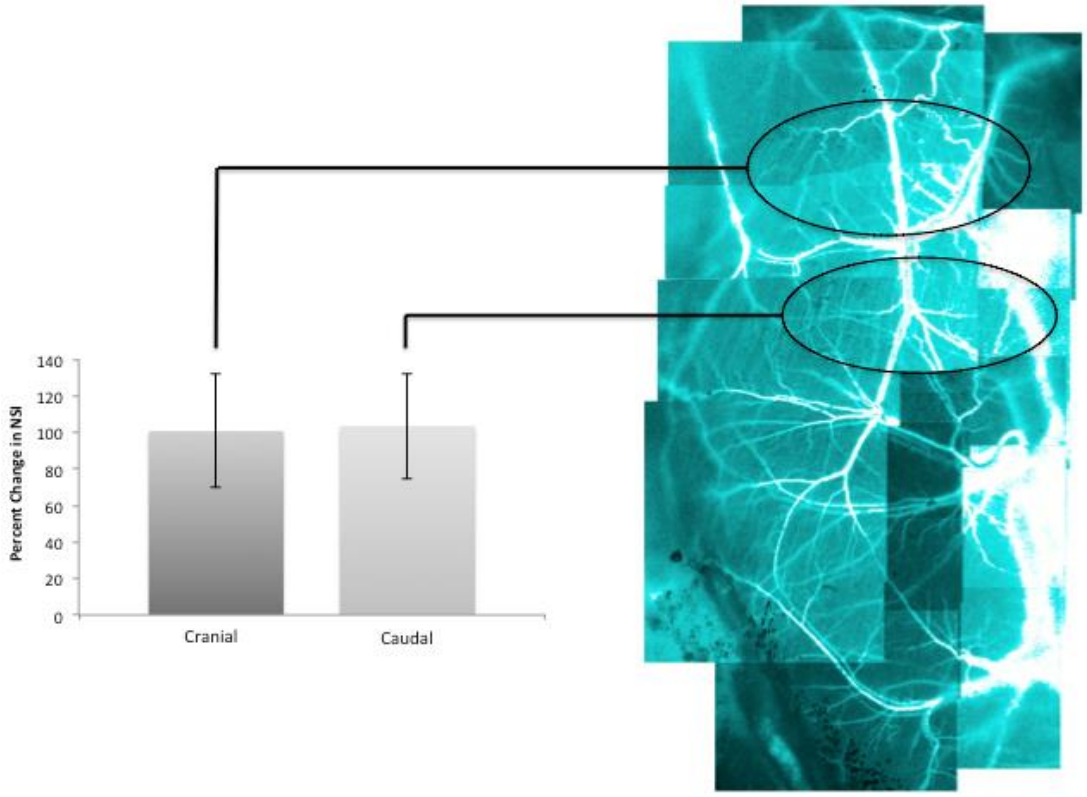

Figure 20. Percent Changes in Normalized Speckle Intensity by Region. Percent changes in NSI show comparable increases in response to SNP in the cranial (n=4) and caudal (n=9) regions of the ischemic tree 21 days post-ligation.

Appendix D

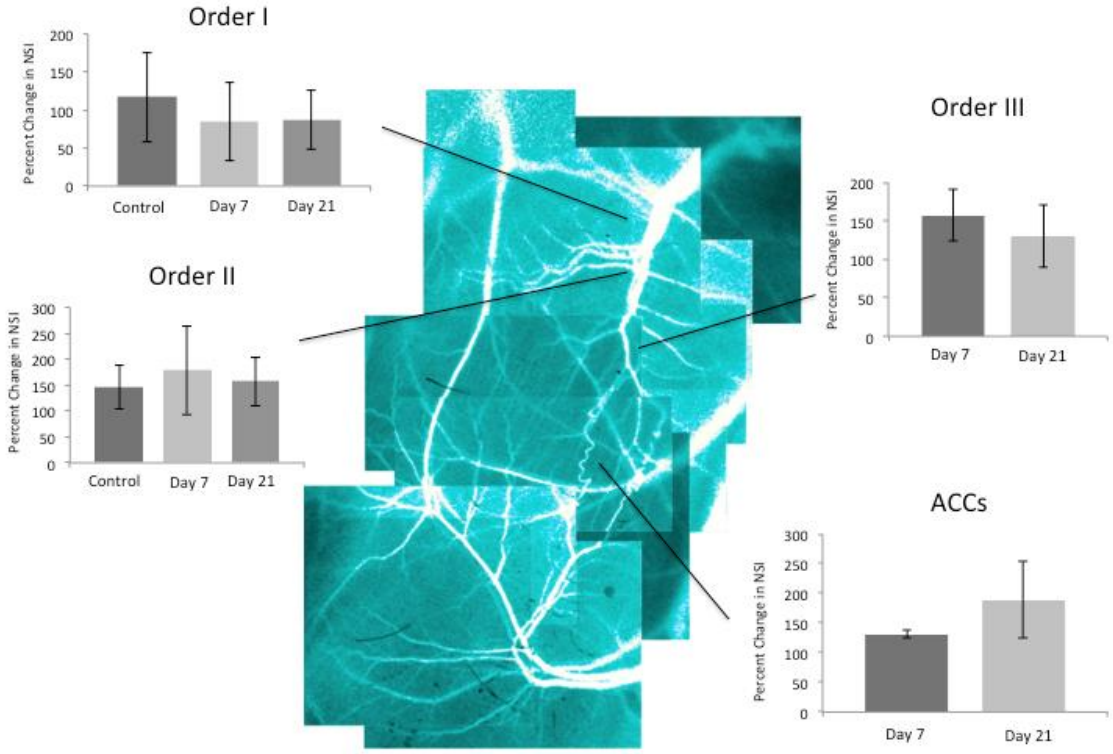

Figure 21. Percent Changes in Normalized Speckle Intensity by Branch Order. Percent changes in NSI amongst different ordered vessels throughout the ischemic tree show comparable increases in response to SNP at each order. Order I: control (n=4), day 7 (n=2), day 21 (n=5); Order 2: control (n=11), day 7 (n=3), day 21 (n=8); Order 3: day 7 (n=2), day 21 (5); ACCs: day 7 (n=2), day 21 (n=3).

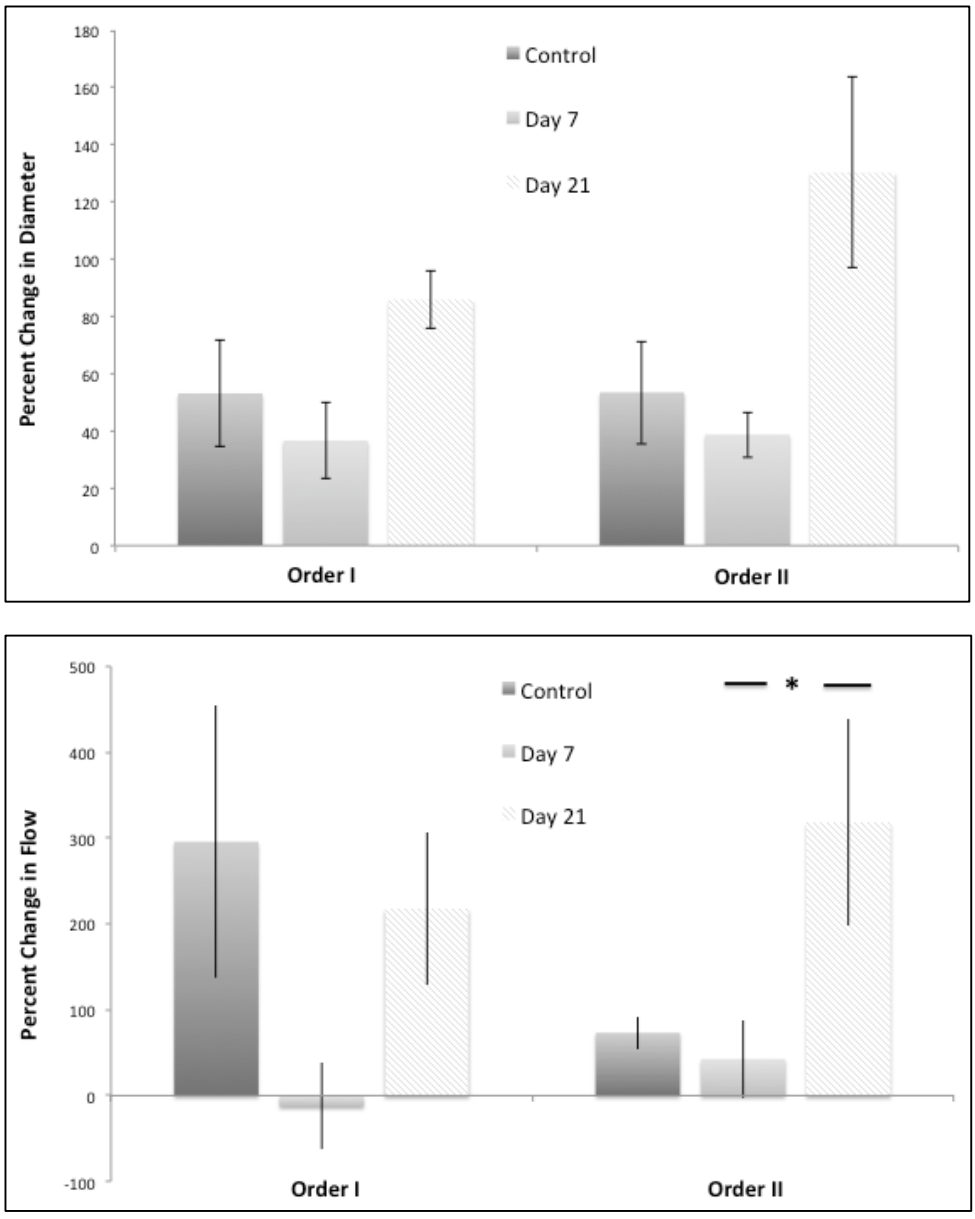

Figure 22. Percent Changes in Blood Flow by Branch Order. Characterization of changes in blood flow by first-order (control, n=3; day 7, n=2; day 21, n=3) and second-order vessels (control, n=4; day 7, n=6; day 21, n=5).

Appendix E

```
// Spatial LASCA: 3x3 spatial window
//Using OpenCV libraries
int _tmain(int argc, _TCHAR* argv[])
{
	for (int l = 1; l <= 55; l++){
	   string String = static_cast<ostringstream*>(&(ostringstream() << l))->str();
	   string str = "14-1-000" + String;
	   Mat img = imread(path + "\\" + str + ".tif", -1);
	   img.convertTo(img, CV_32F);
	   float *ptrimg = (float *)(img.data);

	   std::vector<float> temporalRow;
	   float *outputimg = (float*)malloc(img.rows*img.cols*sizeof(float));

	   for (int i = 1; i < (img.rows - 1); i++) {
		for (int j = 1; j < (img.cols - 1); j++) {
			for (int m = (i - 1); m <= (i + 1); m++) {
				for (int n = (j - 1); n <= (j + 1); n++) {

					int roiIndex = m*img.cols + n;

					temporalRow.push_back(ptrimg[roiIndex]);
				}
			}
			cv::Scalar_<float> temporalMean = mean(temporalRow);
			pow(temporalRow, 2, temporalRow);
			cv::Scalar_<float> temporalMeanSqr = mean(temporalRow);
			outputimg[i*img.cols + j] = (float)((temporalMeanSqr[0] - (temporalMean[0] *
			temporalMean[0])) / temporalMean[0]);
			vector<float>().swap(temporalRow);
		}
	   }
	   cout << outputimg[50 * img.cols + 50] << endl;
	   Mat contrastimg(img.rows, img.cols, CV_32F, outputimg);
	   img.release();
	   cout << contrastimg.at<float>(50, 50) << endl;
	   contrastimg.convertTo(contrastimg, CV_16U);
	   imwrite(outputpath + "\\" + String + ".tiff", contrastimg);
	   free(outputimg);
	   contrastimg.release();
	}
}
```

```
// Temporal LASCA: 15 image temporal window
//Using OpenCV libraries
int _tmain(int argc, _TCHAR* argv[])
{
	std::vector<float> temporalRow;
	float *outputimg = (float*)malloc(img1.rows*img1.cols*sizeof(float));

	for (int i = 1; i < (img1.rows - 1); i++) {
	   for (int j = 1; j < (img1.cols - 1); j++) {

			int roiIndex = i*img1.cols + j;

			temporalRow.push_back(ptrimg1[roiIndex]);
			temporalRow.push_back(ptrimg2[roiIndex]);
			temporalRow.push_back(ptrimg3[roiIndex]);
			temporalRow.push_back(ptrimg4[roiIndex]);
			temporalRow.push_back(ptrimg5[roiIndex]);
			temporalRow.push_back(ptrimg6[roiIndex]);
			temporalRow.push_back(ptrimg7[roiIndex]);
			temporalRow.push_back(ptrimg8[roiIndex]);
			temporalRow.push_back(ptrimg9[roiIndex]);
			temporalRow.push_back(ptrimg10[roiIndex]);
			temporalRow.push_back(ptrimg11[roiIndex]);
			temporalRow.push_back(ptrimg12[roiIndex]);
			temporalRow.push_back(ptrimg13[roiIndex]);
			temporalRow.push_back(ptrimg14[roiIndex]);
			temporalRow.push_back(ptrimg15[roiIndex]);

			cv::Scalar_<float> temporalMean = mean(temporalRow);
			pow(temporalRow, 2, temporalRow);
			cv::Scalar_<float> temporalMeanSqr = mean(temporalRow);
			outputimg[i*img1.cols + j] = (float)((temporalMeanSqr[0] - (temporalMean[0] *
			temporalMean[0])) / temporalMean[0]);
			vector<float>().swap(temporalRow);
	   }
	}
	cout << outputimg[50 * img1.cols + 50] << endl;
	Mat contrastimg(img1.rows, img1.cols, CV_32F, outputimg);
	cout << contrastimg.at<float>(50, 50) << endl;
	contrastimg.convertTo(contrastimg, CV_16U);
	imwrite(outputpath + "\\" + "tLASCA 15 result" + ".tiff", contrastimg);
}
```

```
//Spatio-temporal LASCA: 3x3 spatial window and 15 image temporal window
//Using OpenCV libraries
int _tmain(int argc, _TCHAR* argv[])
{
std::vector<float> temporalRow;
float *outputimg = (float*)malloc(img1.rows*img1.cols*sizeof(float));

        for (int i = 1; i < (img1.rows - 1); i++) {
           for (int j = 1; j < (img1.cols - 1); j++) {
                        for (int m = (i - 1); m <= (i + 1); m++) {
                                for (int n = (j - 1); n <= (j + 1); n++) {

                                        int roiIndex = m*img1.cols + n;

                                        temporalRow.push_back(ptrimg1[roiIndex]);
                                        temporalRow.push_back(ptrimg2[roiIndex]);
                                        temporalRow.push_back(ptrimg3[roiIndex]);
                                        temporalRow.push_back(ptrimg4[roiIndex]);
                                        temporalRow.push_back(ptrimg5[roiIndex]);
                                        temporalRow.push_back(ptrimg6[roiIndex]);
                                        temporalRow.push_back(ptrimg7[roiIndex]);
                                        temporalRow.push_back(ptrimg8[roiIndex]);
                                        temporalRow.push_back(ptrimg9[roiIndex]);
                                        temporalRow.push_back(ptrimg10[roiIndex]);
                                        temporalRow.push_back(ptrimg11[roiIndex]);
                                        temporalRow.push_back(ptrimg12[roiIndex]);
                                        temporalRow.push_back(ptrimg13[roiIndex]);
                                        temporalRow.push_back(ptrimg14[roiIndex]);
                                        temporalRow.push_back(ptrimg15[roiIndex]);
                                }
                        }
                        cv::Scalar_<float> temporalMean = mean(temporalRow);
                        pow(temporalRow, 2, temporalRow);
                        cv::Scalar_<float> temporalMeanSqr = mean(temporalRow);
                        outputimg[i*img1.cols + j] = (float)((temporalMeanSqr[0] - (temporalMean[0] *
                        temporalMean[0])) / temporalMean[0]);
                        vector<float>().swap(temporalRow);
           }
        }
        Mat contrastimg(img1.rows, img1.cols, CV_32F, outputimg);
        contrastimg.convertTo(contrastimg, CV_16U);
        imwrite(outputpath + "\\" + "stLASCA 3x3x15 result" + ".tiff", contrastimg);
        contrastimg.release();
}
```

Appendix F

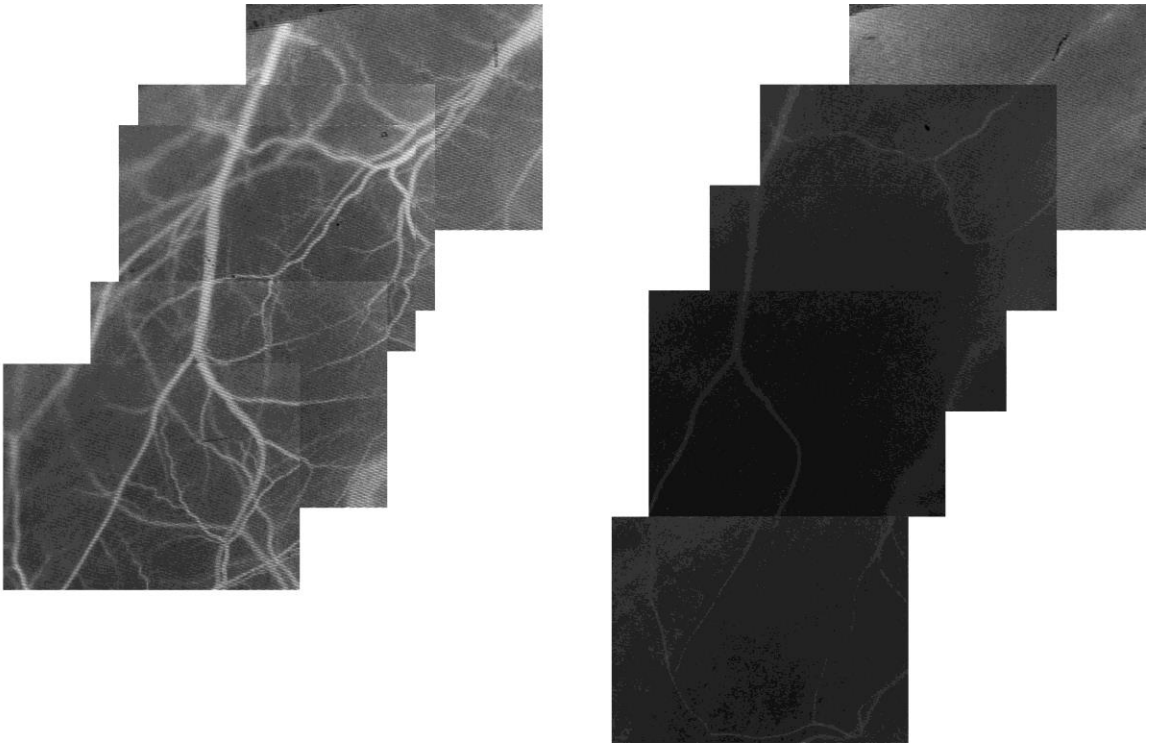

Figure 23. Day 21 Montage 1. Day 21 laser speckle montage; resting on right, dilated on left.

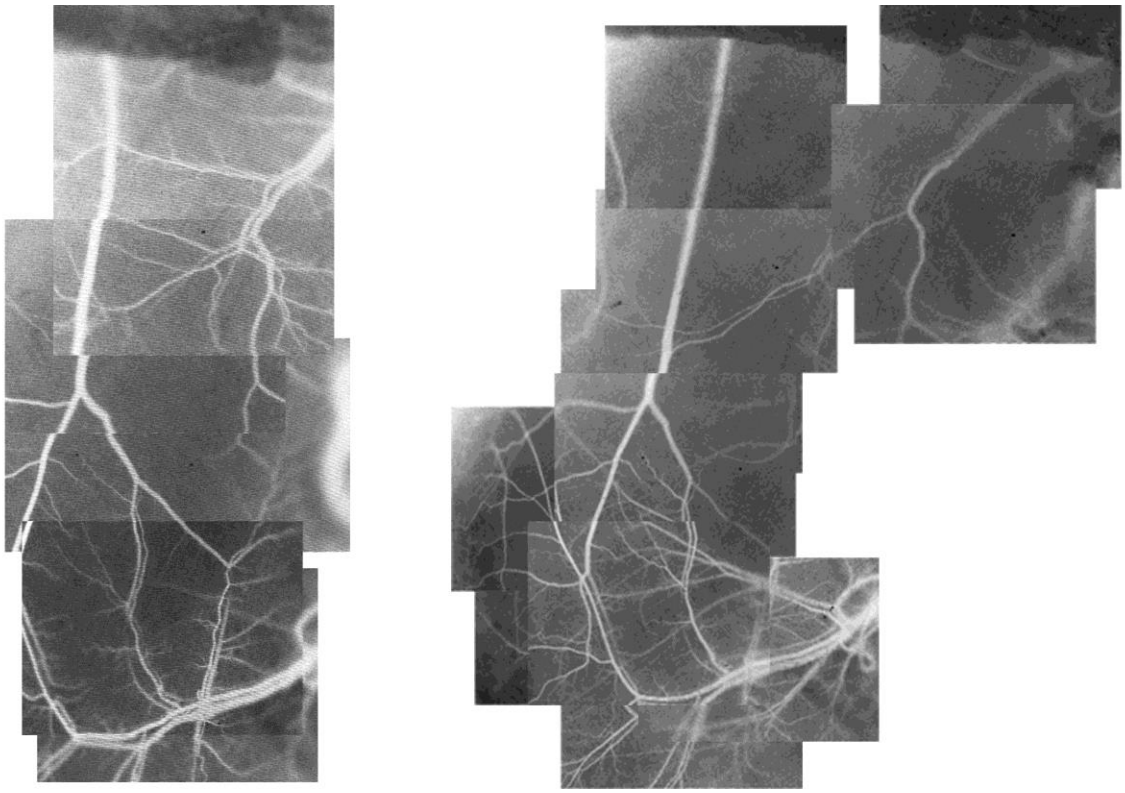

Figure 24. Day 21 Montage 2. Day 21 laser speckle montage; resting on right, dilated on left.

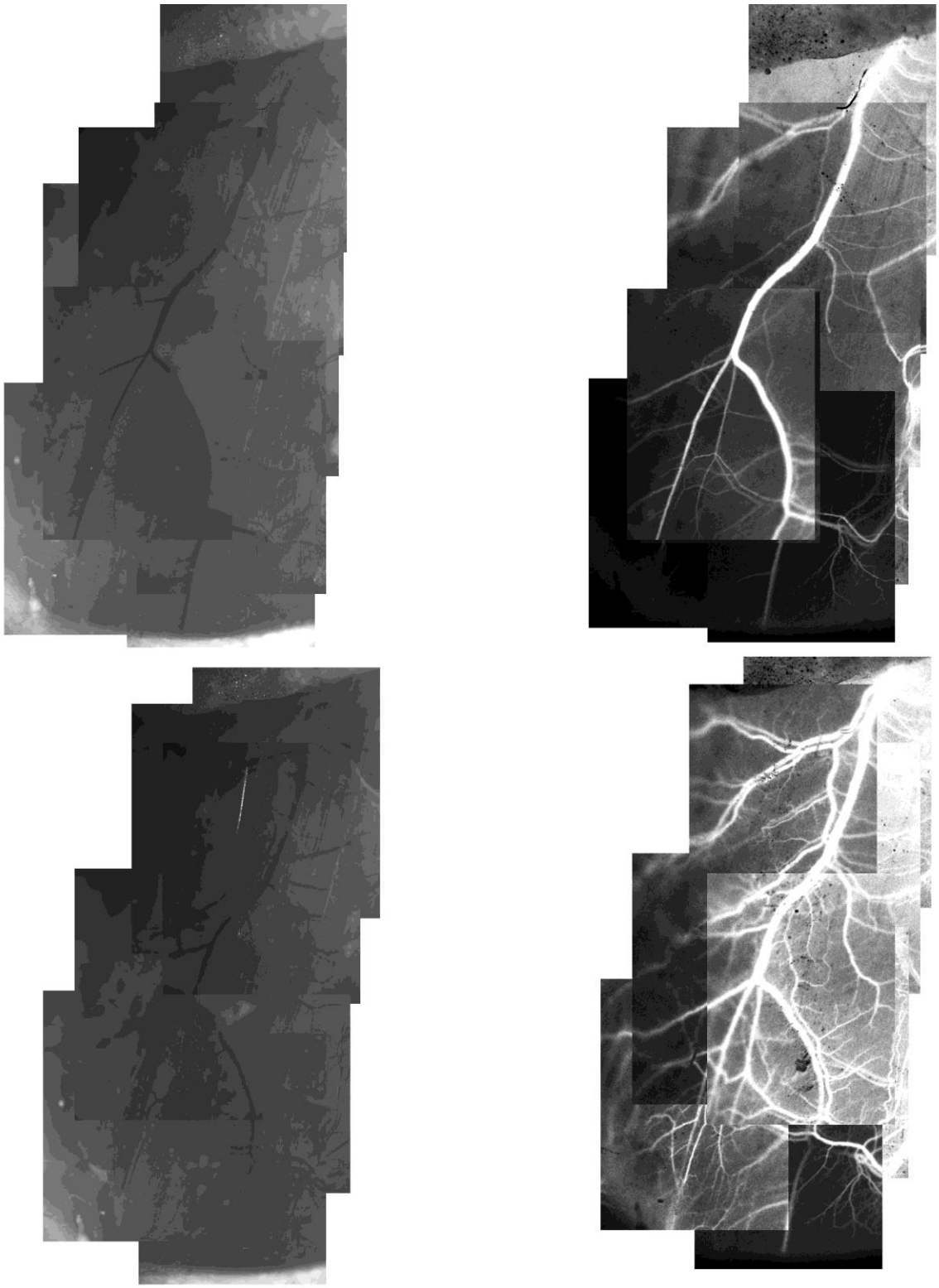

Figure 25. Day 21 Montage 3. Day 21 bright field (left) and laser speckle (right) montages; resting on top, dilated on bottom.

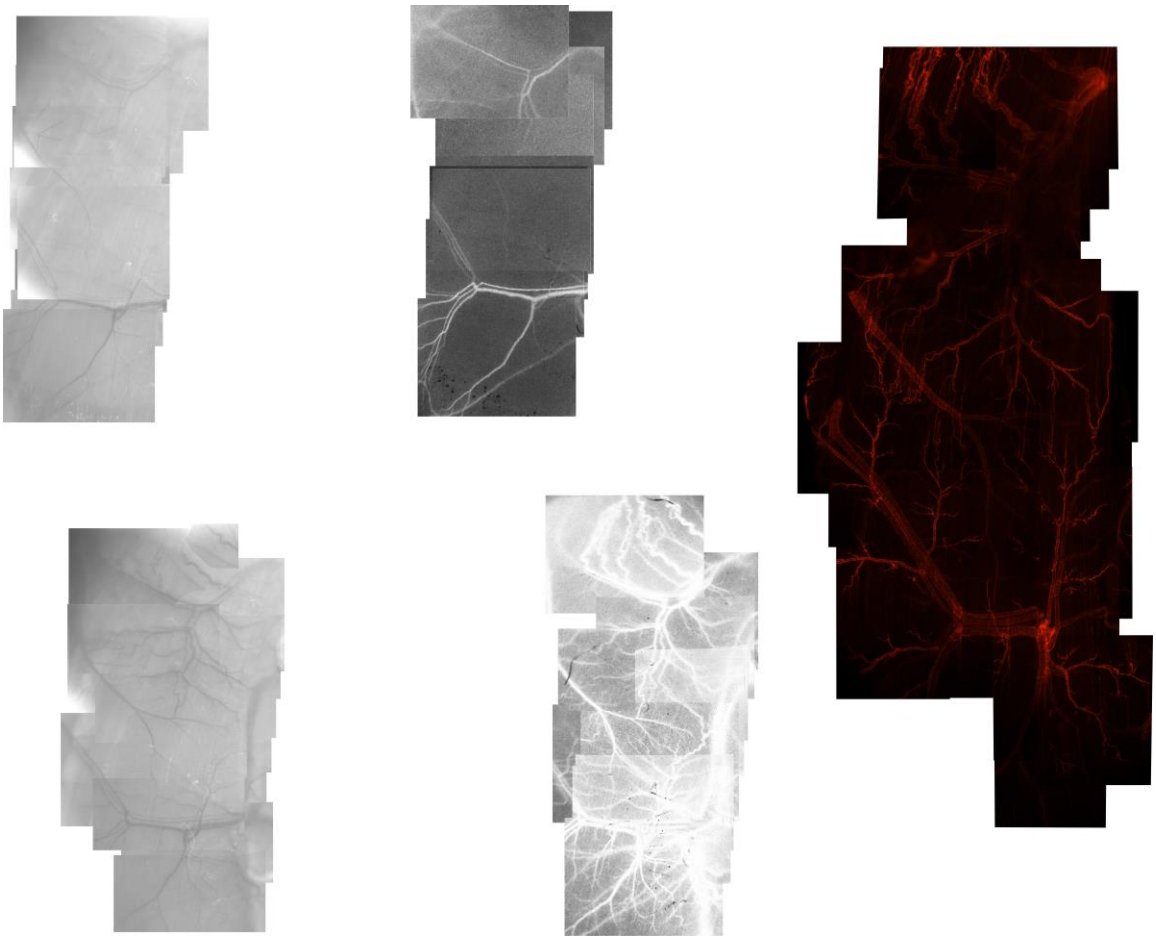

Figure 26. Day 21 Montage 4. Day 21 bright field (left), laser speckle (middle), and α-smooth muscle actin (right) montages; resting on top, dilated on bottom.

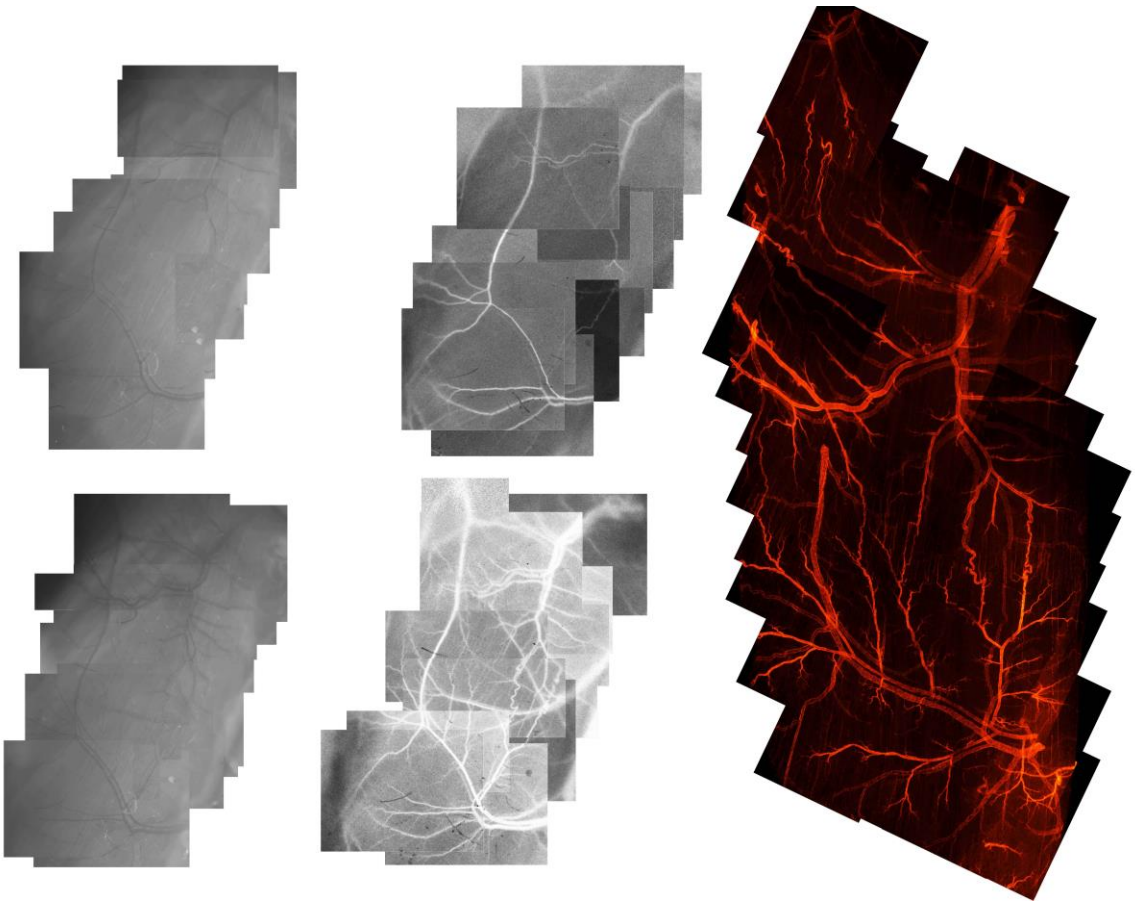

Figure 27. Day 21 Montage 5. Day 21 bright field (left), laser speckle (middle), and α-smooth muscle actin (right) montages; resting on top, dilated on bottom.

Appendix G

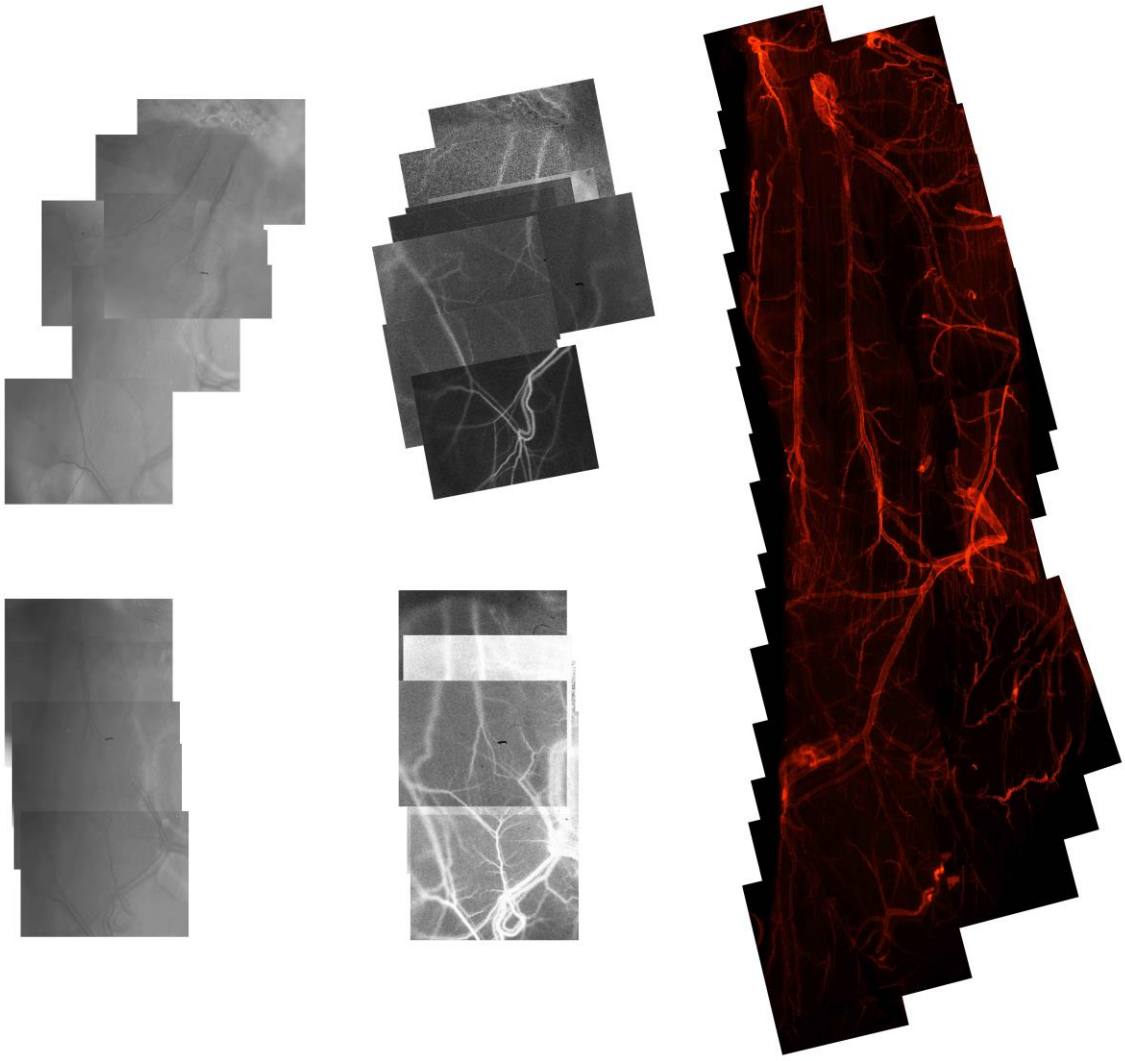

Figure 28. Day 7 Montage 1. Day 7 bright field (left), laser speckle (middle), and α-smooth muscle actin (right) montages; resting on top, dilated on bottom.

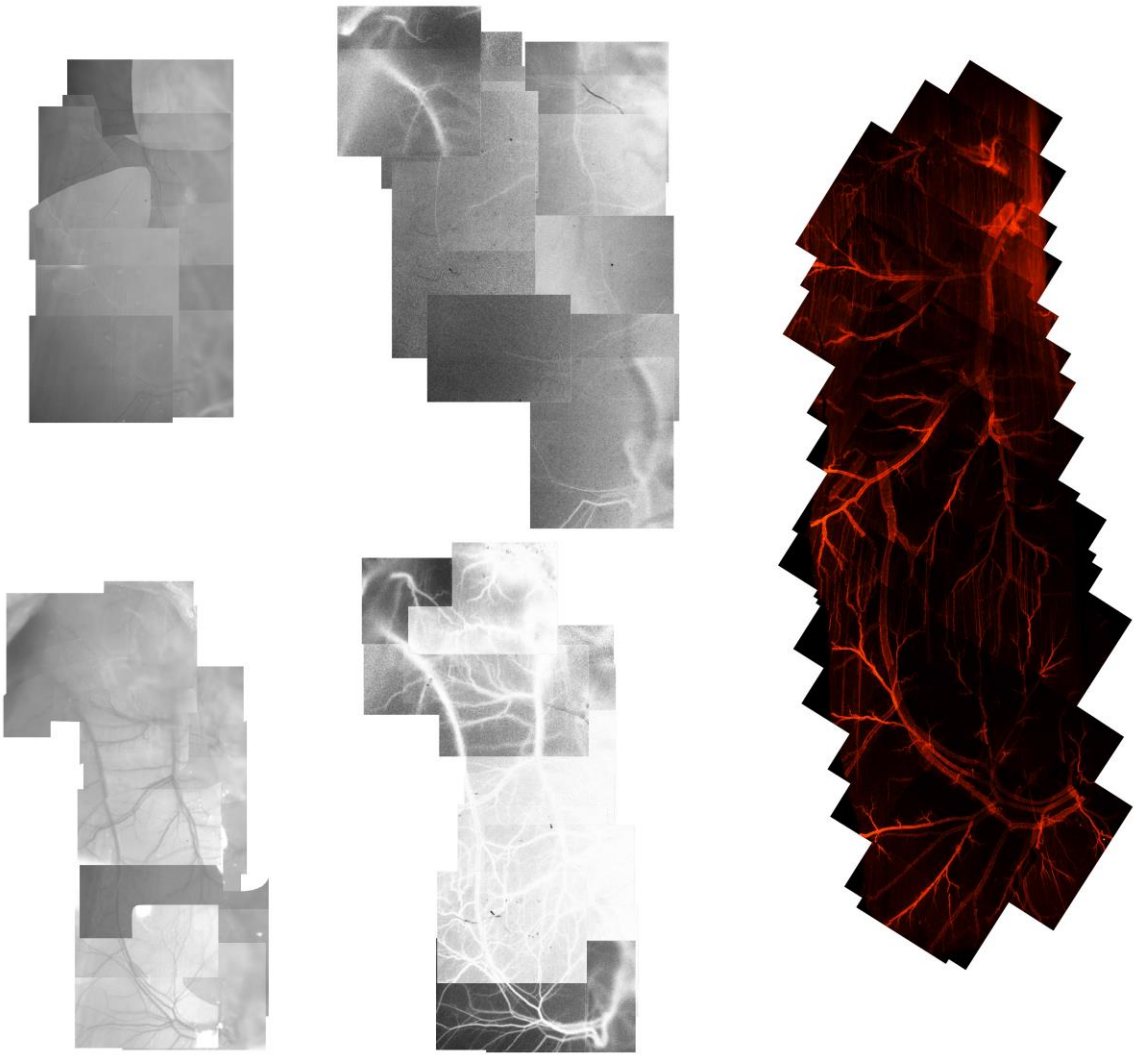

Figure 29. Day 7 Montage 2. Day 7 bright field (left), laser speckle (middle), and α-smooth muscle actin (right) montages; resting on top, dilated on bottom.

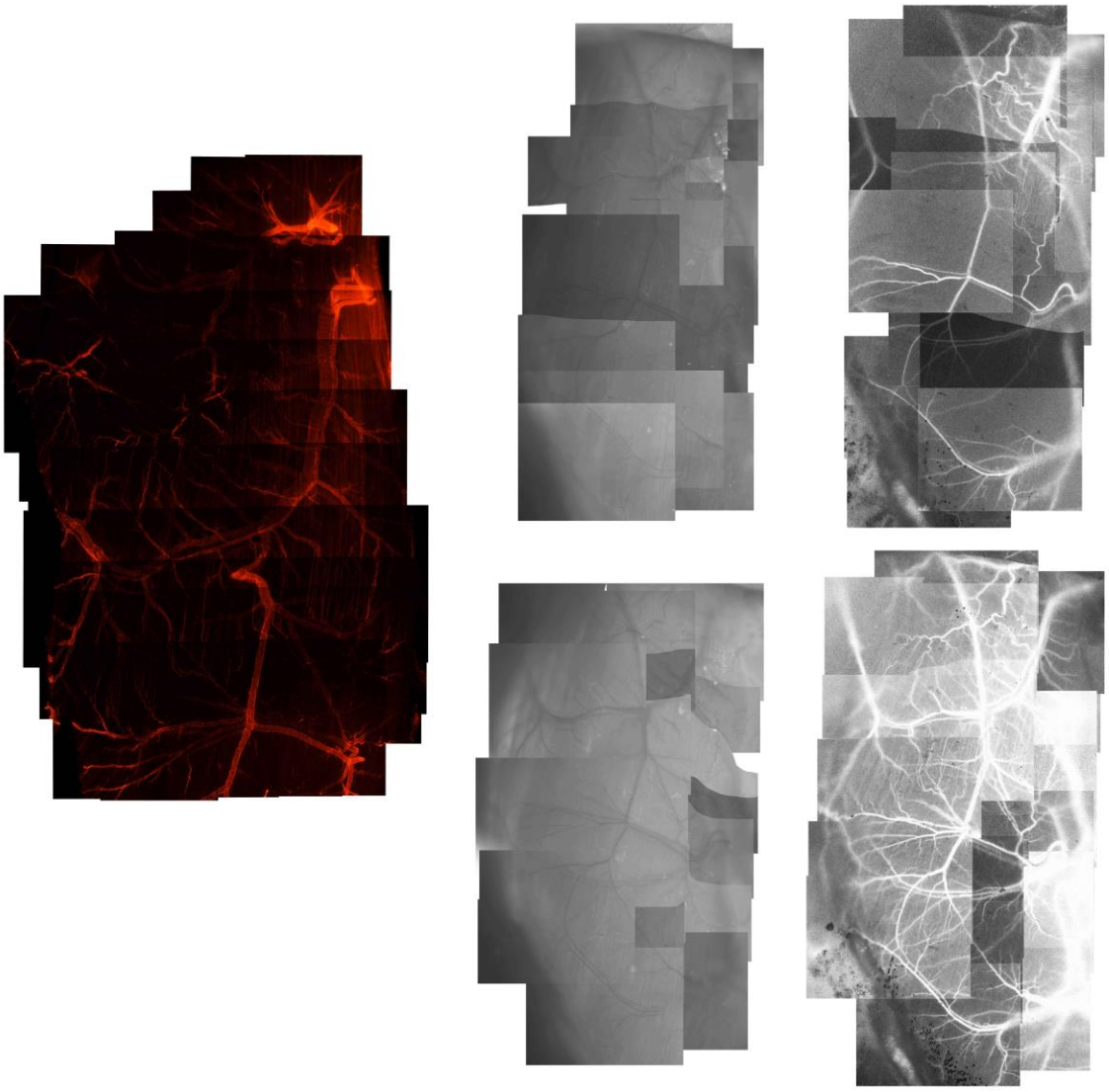

Figure 30. Day 7 Montage 3. Day 7 α-smooth muscle actin (left), bright field (middle), and laser speckle (right) montages; resting on top, dilated on bottom.